1 **Field assessments on impact of CO_2 concentration fluctuations along with complex**

2 **terrain flows on the estimation of the net ecosystem exchange of temperate forests**

3 Dexiong Teng[1,2], Jiaojun Zhu[1,2,3,*], Tian Gao[1,2,3], Fengyuan Yu[1,2], Yuan Zhu[1,2], Xinhua

4 Zhou[3,4], Bai Yang[4]

5 1 CAS Key Laboratory of Forest Ecology and Silviculture, Institute of Applied Ecology, Chinese

6 Academy of Sciences, Shenyang 110000, China

7 2 Qingyuan Forest CERN, National Observation and Research Station, Liaoning Province,

8 Shenyang 110016, China

9 3 CAS-CSI Joint Laboratory of Research and Development for Monitoring Forest Fluxes of Trace

10 Gases and Isotope Elements, Institute of Applied Ecology, Chinese Academy of Sciences,

11 Shenyang 110016, China

12 4 Campbell Scientific Incorporation, Logan, Utah 84321, USA

13 *** Corresponding Author: Jiaojun Zhu**

14 Tel : +86 24 83970342

15 Email: jiaojunzhu@iae.ac.cn

Abstract

The CO_2 storage (F_s) is the cumulation or depletion in CO_2 amount over a period in an ecosystem. Along with the eddy-covariance flux and wind-stream advection of CO_2, it is a major term in the net ecosystem CO_2 exchange (NEE) equation and even dominates in the equation under a stable atmospheric stratification while this equation is used for forest ecosystems over complex terrains. However, estimating the F_s remains challenging due to the frequent gusts and random fluctuations in boundary-layer flows that arouse tremendous difficulties in catching the true trend of CO_2 changes for its storage estimation from eddy-covariance along with the atmospheric profile techniques. Using the measurements from Qingyuan Ker Towers equipped with NEE instrument systems separately covering mixed-broadleaf, oak, and larch forests towers in a mountain watershed, this study investigates the gust periods and CO_2 fluctuation magnitudes while examining their impact on F_s estimation in relation to the terrain complexity index (TCI). The gusts induce CO_2 fluctuations at numerous periods of 1 to 10 min over two hours. Diurnal, seasonal, and spatial differences ($P < 0.01$) in the maximum amplitude of CO_2 fluctuations (A_m) ranges from 1.6 to 136.7 ppm and these difference in a period (P_m) at the same significant level ranges 140 to 170 second. The A_m and P_m are significantly correlated to the magnitude and random error of F_s with diurnal and seasonal differences. These correlations decrease as CO_2 averaging time windows becomes longer. To minimize the uncertainties of F_s, a constant [CO_2] averaging time window for the F_s estimates is not ideal. Dynamic averaging time windows and a decision-level fusion model can reduce the potential underestimation of

38 F_s by 29%–33% for temperate forests in complex terrains. The relative contribution of

39 F_s to the 30-min NEE observations ranged from 17% to 82% depending on turbulent

40 mixing and TCI. The study's approach is notable as it incorporates TCI and utilizes

41 three flux towers for replication, making the findings relevant to similar regions with a

42 single tower.

43 **Keywords**: Eddy covariance, complex terrain, carbon flux, storage term, carbon

44 dioxide concentration, random uncertainty

45 **1 Introduction**

46   The accurate estimation of the net ecosystem exchange (NEE) of carbon dioxide

47 (CO_2) in forest ecosystems is crucial for a comprehensive understanding of the global

48 carbon cycle. The eddy covariance (EC) technique has been widely used in forest

49 ecosystems due to its capacity to directly measure the NEE while measurement

50 conditions satisfy the underlying theory. The EC technique is based on a simplified

51 mass conservation equation (after the Reynolds averaging), given by:

$$\text{NEE} = \underbrace{\frac{1}{V_m}\int_0^h \left(\frac{\partial \overline{c}}{\partial t}\right)dz}_{\text{I}} + \underbrace{\frac{1}{V_m}\left(\overline{w'c'}\right)_h}_{\text{II}}$$

52
$$+ \underbrace{\frac{1}{V_m}\int_0^h \left(\overline{w}(z)\frac{\partial \overline{c}}{\partial z} + \overline{c}(z)\frac{\partial \overline{w}}{\partial z}\right)dz}_{\text{III}a \qquad\quad \text{III}b},\tag{1}$$

$$+ \underbrace{\frac{1}{V_m}\int_0^h \left(\overline{u}(z)\frac{\partial \overline{c}}{\partial x} + \overline{v}(z)\frac{\partial \overline{c}}{\partial y}\right)dz}_{\text{IV}}$$

53 where V_m is the volume of dry air in the control volume; c is the CO_2 mixing ratio; t is

54 the time; h is the measure height; u, v, and w denote the velocity components in the x,

y, and z directions, respectively; and an overbar denotes Reynolds averaging. This equation conceptualizes the NEE within a control volume from the ground to the measurement height (h), while ignoring the horizontal turbulence term divergence (Feigenwinter et al., 2004). In this equation, term I is the CO_2 storage (F_s) representing the change in the average CO_2 concentration (hereafter [CO_2]). Terms II, IIIa, IIIb, and IV represent the vertical turbulent flux (F_c), the vertical advection, the interface vertical mass advection, such as the evaporation process (Webb et al., 1980), and the horizontal advection, respectively.

Most flux measurements typically lack the solutions for terms III and IV, and can only estimate the NEE by summing F_c and F_s, and even a significant number of sites ignored the F_s. The F_s in the vertical gas column within a canopy can be substantial, requiring attention in NEE estimates (Aubinet et al., 2000). The F_s contributes ~60% to nocturnal turbulent flux underestimation in forest ecosystems with "ideal" topography (Mchugh et al., 2017). Especially, during atmospherically stable periods such as the early morning, sunset, and nighttime transitions, the F_s has a significant impact on the NEE. For 30-min ecosystem carbon flux measurements, ignoring F_s would underestimate the NEE (Zhang et al., 2010). The F_s value typically ranges from -2 to -5 $\mu mol\ m^{-2}\ s^{-1}$ in the early morning, and the F_s is about 1–3 $\mu mol\ m^{-2}\ s^{-1}$ after sunset for temperate forests. The effect of the F_s on the NEE of forest ecosystems decreases with the increase of timescale (Li et al., 2020). However, neglecting the F_s value can lead to a misunderstanding of the CO_2 exchange processes, such as ecosystem respiration and photosynthesis, and their relationship with key control factors such as

solar radiation, temperature, and moisture (Mchugh et al., 2017). Therefore, it is imperative not to overlook F_s to ensure more precise NEE estimates of forest ecosystems, particularly in complex terrains.

Despite the challenges inherent in monitoring forest conditions, understanding the carbon flux of forest ecosystems in complex terrains or with heterogeneous underlying surfaces remains an area of great interest. Topography complexity plays a complex role in the transportation of momentum, energy, and mass in the atmospheric boundary layer, with direct impacts on the airflow patterns, spatiotemporal characteristics, and gas concentration fluctuations (Sha et al., 2021; Finnigan et al., 2020). Differences in airflow along the slope, lateral CO_2 discharge downhill, and spatiotemporal variations in soil respiration result in the CO_2 outflow from slopes and valleys lagging behind the flat top of the mountain (De Araújo et al., 2010). At night, under stable atmospheric stratification, cold air moves from valley forest canopy to the ground the and then flows to low-lying areas, causing a "carbon pooling" effect. The gradient of [CO_2] below the EC sensors fluctuates significantly, and the cold air discharge above the canopy reduces CO_2 storage, leading to an underestimation of forest ecosystem respiration (Yao et al., 2011; De Araújo et al., 2008; De Araújo et al., 2010).

According to the theoretical definition, F_s estimates are derived by averaging the [CO_2] of the control volume at the beginning and the end of the EC averaging period (30 min or 1 h) and dividing by the EC averaging period (Finnigan, 2006). The estimation of F_s at numerous sites frequently employs a vertical profile system. This approach operates under the assumption that the F_s represents the integration of the time

derivative of the vertically determined column-averaged $[CO_2]$. It is noteworthy that the column-averaged $[CO_2]$ may not accurately represent the average $[CO_2]$ of the control volume in cases of inadequate air mixing, leading to insufficient sampling. Previous study showed that relying solely on tower-top measurements can lead to underestimation of F_s by up to 34% compared to the eight-level profile approach (Gu et al., 2012). The NEE magnitude with the F_s based on the 2-min $[CO_2]$ averaging time window (instantaneous concentration approach) was found to be 5% higher than that of the 30-min-window-based F_s (averaging concentration approach), particularly during nighttime in the growing season (Wang et al., 2016). A proper measuring system with improving the horizontal representativeness can reduce the bias of F_s to 2–10% (Nicolini et al., 2018). Most research has examined how vertical and horizontal gas concentration sampling point distribution affects the uncertainty in F_s estimation (Bjorkegren et al., 2015; Wang et al., 2016; Yang et al., 2007; Yang et al., 1999), with a small number of studies examining the effect of $[CO_2]$ sampling frequency on the F_s (Finnigan, 2006; Heinesch et al., 2007). Certain studies have experimentally validated new concepts, such as correlating the gas sampling point concentration with the horizontal distribution (Nicolini et al., 2018). Some studies have approached the true value theoretically, such as through defining the control volume represented by flux measurements (Metzger, 2018; Xu et al., 2019). However, the number of complete column samples required to describe the column-averaged $[CO_2]$ of each 30-min or 1-h F_s estimate is still undetermined.

Previous studies have emphasized the significance of the F_s to the NEE and the

influence of [CO_2] dynamics on F_s estimates in complex terrains. To overcome any

disparities between sensors and obtain precise changes in the [CO_2] gradient above and

below the forest canopy, individual gas analyzers are extensively utilized to measure

[CO_2] levels vertically (Siebicke et al., 2011). However, a single gas analyzer introduces

time delays when monitoring multi-point [CO_2] curves. Accurately determining the F_s

estimates can be challenging due to the spatial and temporal resolution of [CO_2]

measurements (Wang et al., 2016). The random error of the F_s estimates using one

complete column sample is considerably high due to short-term [CO_2] fluctuations

(Nicolini et al., 2018). The calculation of the F_s using time-averaged [CO_2] profiling

leads to significant information loss at high frequency, resulting in a substantial

underestimation bias. Furthermore, time-averaged [CO_2] profiling is employed to

represent the [CO_2] average within control volume due to resource constraints. This

leads to the gap that the systematic bias and random error in F_s estimate are

irreconcilable. This issue necessitates further efforts to characterize [CO_2] fluctuations

across different sites and demonstrate the mechanisms influencing F_s magnitudes,

uncertainties, and their contributions to NEE observations in complex terrains. Thus,

this study aims to bridge this gap by introducing a statistical method to estimate F_s

values and their uncertainties.

This paper employed an innovative EC experimental setup with three flux towers

(Qingyuan-Ker Towers) to monitor three typical types of temperate forest stands

located in complex terrains in northeastern China. This study introduces a decision-

level fusion model based on weighing the underestimation bias and random error of the

143   F_s to obtain more accurate results. The objectives of this study were to: 1) compare

144   diurnal, seasonal, and spatial differences in $[CO_2]$ fluctuations, F_s, and its uncertainty;

145   2) examine the variation in F_s uncertainty with different $[CO_2]$ averaging time windows;

146   and 3) investigate the response of F_s and its uncertainty to $[CO_2]$ fluctuations, wind

147   above the canopy, and terrain complexity, and quantify the impact of the F_s on the NEE

148   estimates under these conditions.

149   **2 Materials and methods**

150   2.1 Study site and instrumental set-up

151   This study was conducted in temperate forests in a watershed based on the Ker

152   towers (Zhu et al., 2021; Gao et al., 2020), situated in northeast China (41°50′N,

153   124°56′E). The region experiences a temperate continental monsoon climate, with an

154   average annual temperature of 4.3 °C and annual rainfall of 758 mm from 2010 to 2021

155   (Li et al., 2023). The Ker towers consist of three 50-m-high EC towers (Fig. 1) that

156   observe a mixed broadleaved forest (MBF), a Mongolian oak forest (MOF), and a Larch

157   plantation forest (LPF).
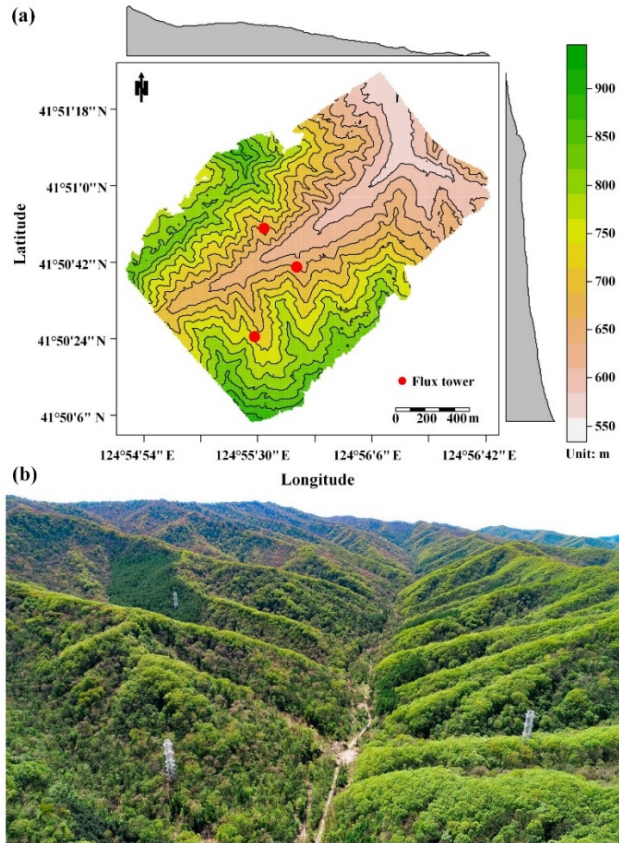
159 Fig. 1 Overview of the study area. The first map (a) depicts the topography of the study site, with

160 black curves indicating elevation contours, and marginal distributions represented as a gray graph,

161 averaged over rows and columns. The second image (b) features an aerial photograph of the

162 Qingyuan-Ker towers captured in the growing season (Gao et al., 2020).

163 The basic information regarding Ker towers in this study is presented in Table 1.

164 The CPEC310 integrated system from Campbell Scientific comprising an EC155

165 closed-path infrared gas analyzer (IRGA) and a CSAT3A sonic anemometer, was

166 employed to monitor the three-dimensional wind speed and CO_2/H_2O concentrations

167 (10 Hz). The atmospheric profiling system (AP200, Campbell Scientific Ltd., Logan,

168 UT, USA) was utilized to measure the CO_2/H_2O concentrations with eight height levels.

169 Each level was measured for 15 s (with 10 s for the flushing of the manifold and 5 s for

170 logging the average), leading to a measurement cycle of 2 min. Due to calibration, filter

171 changes, and rugged weather, 10% CPEC data and 3% AP200 data were missed in our

172

173 Table 1 Basic information of Ker towers

Forest	Mixed broad-leaved	Mongolian oak	Larch plantation
Experiment period	Jan 01, 2020–Dec 31, 2021	Jan 01, 2020–Dec 31, 2021	Jan 01, 2020–Dec 31, 2021
Elevation (m)	634	669	721
Slope (°)	14.8 ± 2.1	19.1 ± 2.9	16.2 ± 5.3
Canopy height (m)	21.5 ± 1.8	13.9 ± 0.6	19.5 ± 0.6
Leaf area indices	3.0 ± 0.5	3.1 ± 0.8	3.9 ± 0.6
Eddy covariance system	CPEC310	CPEC310	CPEC310
Eddy covariance sensor height (m)	46	46	36
Atmospheric profiling system	AP200	AP200	AP200
Profile heights (m)	0.5, 2, 6, 11, 16, 21, 26, 36	0.5, 2, 6, 11, 16, 21, 26, 36	0.5, 2, 6, 11, 16, 21, 26, 36

174 2.2 Calculation of storage flux

175   Averaging the [CO_2] in a time window was utilized to calculate the F_s values, in

176 addition to data on the air pressure, CO_2/H_2O molar fractions, and air temperature at

177 different heights above the ground surface (Finnigan, 2006; Montagnani et al., 2018;

178 Xu et al., 2019). The molar mixing ratio and mass mixing ratio are conserved quantities

179 with the variation of air temperature, air pressure, and water vapor concentration,

180 whereas the molar fraction is not. This study determined the F_s using the molar mixing

181 ratio obtained from CO_2/H_2O molar fraction observations, applying the ideal gas law

182 and Dalton's partial pressure law (Montagnani et al., 2009). The water vapor molar

183 mixing ratio (χ_v) in mmol mol^{-1} is given by

$$\chi_v = \frac{c_v}{1 - c_v \times 10^{-3}}, \tag{2}$$

where c_v is the water vapor molar fraction in mmol mol^{-1}, and the CO_2 molar mixing

ratio (χ_c) in μmol mol^{-1} is given by

$$\chi_c = \frac{c_c}{1 - c_v \times 10^{-3}}, \tag{3}$$

where c_c is the CO_2 molar fraction in μmol mol^{-1}.

The dry air density ($\bar{\rho}_d$) in mol m^{-3} is calculated as follows:

$$\bar{\rho}_d = \frac{\bar{P}}{(\bar{T} + 273.15) \times (R^* + \chi_v \times 10^{-3} \cdot R^* \cdot M_d/M_v)}, \tag{4}$$

where R^* is the air gas constant (8.31441 Pa m^3 K^{-1} mol^{-1}), $\bar{P}$ is the air pressure in

Pa, and $\bar{T}$ is the average air temperature in Celsius. M_d and M_v are the dry air and

water vapor molar mass (18.015 g mol^{-1}), respectively. M_d is calculated from the CO_2

molar mixing ratio (Khélifa et al., 2007):

$$M_d = 28.9635 + M_c \cdot (\chi_c \times 10^{-6} - 0.0004), \tag{5}$$

where M_c is the carbon molar mass (12.011 g mol^{-1}).

The F_s estimated from eight-level profiles are calculated as follows:

$$F_s = \bar{\rho}_d \int_0^h \frac{d\bar{\chi}_c}{dt} dz \doteq \bar{\rho}_d \sum_{i=1}^{8} \frac{\Delta\bar{\chi}_{c_i}\Delta h_i}{\Delta t}, \tag{6}$$

where $\bar{\chi}_c$ is the average CO_2 molar mixing ratio and Δh_i is the height represented by

each level.

When measuring the F_s by sampling CO_2 at several levels using a single analyzer,

the synchronous observations of CO_2 profile are impractical. Consequently, discrete

temporal sampling and time averaging become necessary. To ensure the temporal

alignment of F_s with F_c, the average [CO_2] measurements within the control volume at

the beginning and end (*t*) of an averaging period (30 min) are calculated by averaging

over a time window (τ min) as follows:

$$\bar{\chi}_{c_i} = \frac{2}{\tau} \sum_{t-\frac{\tau}{2} < t \le t + \frac{\tau}{2}} \chi_{c_i}(t), \tag{7}$$

where τ = 4, 8, …, 28 min. Theoretically, the time window should be kept as short as possible in comparison to the turbulence flux averaging period to comply with the principle of Reynolds decomposition. We use large windows here for CO_2 averaging in an attempt to demonstrate the effects of different window sizes on the accuracy of storage flux estimates.

2.3 Data analysis

To evaluate the impact of [CO_2] fluctuations on F_s measurements and its corresponding uncertainty, empirical modal decomposition (EMD) and Fourier spectrum analysis (FSA) were used to extract the period and amplitude of fluctuations in the high-frequency [CO_2] time series (10 Hz). EMD was used to decompose the [CO_2] time series into intrinsic mode functions based on local signal properties (Huang and Wu, 2008), which yield instantaneous frequencies as functions of time, allowing for the identification of embedded structures of eddies. EMD is applicable to non-linear and non-stationary processes (Huang et al., 1998). The period and amplitude of [CO_2] fluctuations above the forest canopies reflected the eddy size. Subsequently, the maximum period and amplitude of [CO_2] fluctuations in a short term (2h) was indicative of large eddies under the influence of gust.

Due to the diurnal and seasonal variability of flux measurements, this study defined the transition period and growing season. The solar elevation angle was used

221 to define the transition period as 1-h before sunrise (sunset) to 2-h after sunrise (sunset).

222 The growing degree days (GDDs) were calculated using the base temperature (T_{base}) to

223 determine the beginning and end of the growing season, and the formula was as follows

224 (Mcmaster and Wilhelm, 1997):

$$GDD = \frac{1}{2}(T_{max} + T_{min}) - T_{base}, \tag{8}$$

225 where T_{base} is 6°C. Considering the persistent demand of temperature to support

226 vegetation growth, the fourth day of the first GDD greater than zero (less than zero)

227 over a span of five consecutive days was defined as the starting (ending) time of the

228 growing season.

229   The main data processing and analysis steps are outlined below:

230   1. EMD and Fourier spectrum analysis of [CO_2] high-frequency time series were

231 used to extract the maximum amplitude (A_m) and corresponding period (P_m) of [CO_2]

232 fluctuations every 2 h. The data were divided into two subsets based on P_m, with a cut-

233 off of 150 s.

234   2. CO_2 storage fluxes were calculated for different [CO_2] averaging time windows

235 (τ), ranging from 4 to 28 min in increments of 4 min.

236   3. The standardized major axis (SMA) regression model (Warton et al., 2012) was

237 used to compare the slope differences (bias) between F_{s_τ} and F_{s_28} for different P_m and

238 the forest stands. The SMA model offers routines for comparing parameters a and b

239 among groups for symmetric problems.

240   4. The normalized root mean square error (NRMSE) and slope were used to

241 evaluate the relative error and bias between F_{s_τ} and F_{s_28}. The NRMSE is calculated as

242   follows:

$$NRMSE = 100 \times \sqrt{\frac{\sum_{i=1}^{N}(F_{s\_\tau}^{(i)} - F_{s\_28}^{(i)})^2}{\sum_{i=1}^{N}(F_{s\_28}^{(i)} - \overline{F_{s\_28}})^2}}, \qquad (9)$$

243   where i indicates the ith observation.

244   5. The normalized weighting coefficient (w) of F_{s_τ} was estimated based on the

245   NRMSE and slope (Wang et al., 2020). The details are shown in Appendix A1. Then,

246   using the decision-level fusion model, F_{s_comb} was calculated as follows:

$$F_{s\_comb} = w_1^* \cdot F_{s\_4} + w_2^* \cdot F_{s\_8} + \cdots + w_7^* \cdot F_{s\_28} \qquad (10)$$

247   The decision-level fusion model automatically assigned weights to the F_s based on

248   different [CO_2] averaging time windows. Its purpose in this study was to balance the

249   relative error and bias of F_s estimates caused by [CO_2] sampling. The analysis was

250   performed using the EMD and smatr R packages (Warton et al., 2012; Huang et al.,

251   1998).

252   2.4 Uncertainty analysis

253   To improve the accuracy of estimating the uncertainty of F_s using individual tower,

254   this work has made modifications to the 24-h difference method by extending the

255   sampling time windows and applying meteorological condition constraints (Hollinger

256   and Richardson, 2005). This method trades time for space to estimate the uncertainty

257   of F_s. To determine the uncertainty of F_s, expressed as $\sigma(\varepsilon_s)$, in this case, we compared

258   the observations at moment i within a day to the average of several observations during

259   a similar period and with similar meteorological conditions. The specific computations

260   were as follows:

$$\overline{F}_s^{(i)} = \frac{1}{N} \sum_{t \in \Omega, \lambda_t \in \Lambda} I(\lambda_t) \cdot F_s^{(t)}, \tag{11}$$

$$\Lambda = \{\lambda_t | \sqrt{\frac{\left(u_*^{(\lambda_t)} - u_*^{(i)}\right)^2}{\sigma_{u_*}} + \frac{(Ta^{(\lambda_t)} - Ta^{(i)})^2}{\sigma_{Ta}} + \frac{(H^{(\lambda_t)} - H^{(i)})^2}{\sigma_H}} < \delta\}, \tag{12}$$

$$\varepsilon_s^{(i)} = F_s^{(i)} - \overline{F}_s^{(i)}, \tag{13}$$

$$\overline{\varepsilon}_s^{(i)} = \frac{1}{N} \sum_{t \in \Omega, \lambda_t \in \Lambda} I(\lambda_t) \cdot \varepsilon_s^{(t)}, \tag{14}$$

$$\sigma(\varepsilon_s)^{(i)} = \sqrt{\frac{1}{N} \sum_{t \in \Omega, \lambda_t \in \Lambda} I(\lambda_t) \cdot (\varepsilon_s^{(t)} - \overline{\varepsilon}_s^{(i)})^2}, \tag{15}$$

261   where Ω was the moment interval (i−0.5 h, i+0.5 h) within a certain time window (15

262   d); I was indicator function; the set Λ represented consisted of elements that meet

263   similar meteorological conditions, including the u_*, air temperature (Ta), and sensible

264   heat flux (H); σ_{u_*}, σ_{Ta}, and σ_H are the standard deviation of the u_*, Ta, and H,

265   respectively; δ was the threshold of Euclidean distance; and ε_s was the random error

266   of Fs.

267   After estimating the uncertainty of Fs, this study extended the work conducted by

268   Richardson et al. (2008) to analyze its relationship with the magnitude of flux

269   measurements (|Fs|), [CO$_2$] fluctuations (A_m and P_m), u_*, and terrain complexity index

270   (TCI). A comprehensible description of the TCI can be found in Appendix A2. This

271   relationship can be approximated by using the following equation:

$$\sigma(\varepsilon_s) = \beta_0 + \sum_{i=1} \beta_i \cdot x_i, \tag{16}$$

272   where the nonzero intercept term β_0 indicates the size of the random uncertainty as

273   x_i approaches 0, which varies with the observation site, with larger value of β_0

274   indicating greater uncertainty. The slope term β_i indicates the sensitivity of the size of

275   the random uncertainty of x_i, with smaller β_i values indicating a probability

276   distribution of uncertainty closer to white noise.

277   **3 Results**

278   3.1 Characterization of [CO_2] fluctuation and F_s variations

279   The [CO_2] high-frequency time series above the forest canopies were decomposed

280   using EMD, followed by spectral analysis to extract the fluctuation period and

281   amplitude of [CO_2] at different time scales. As depicted in Fig. 2, it became evident that

282   the [CO_2] above the canopies displayed short-term fluctuations with periods ranging

283   from 1 to 10 min, and the amplitude of these fluctuations showed an increasing trend

284   with longer periods. This observation strongly suggested the presence of large eddies

285   influenced by gusts above the canopies, and these eddies were responsible for the

286   increasing amplitude of [CO_2] fluctuations as their size increased.
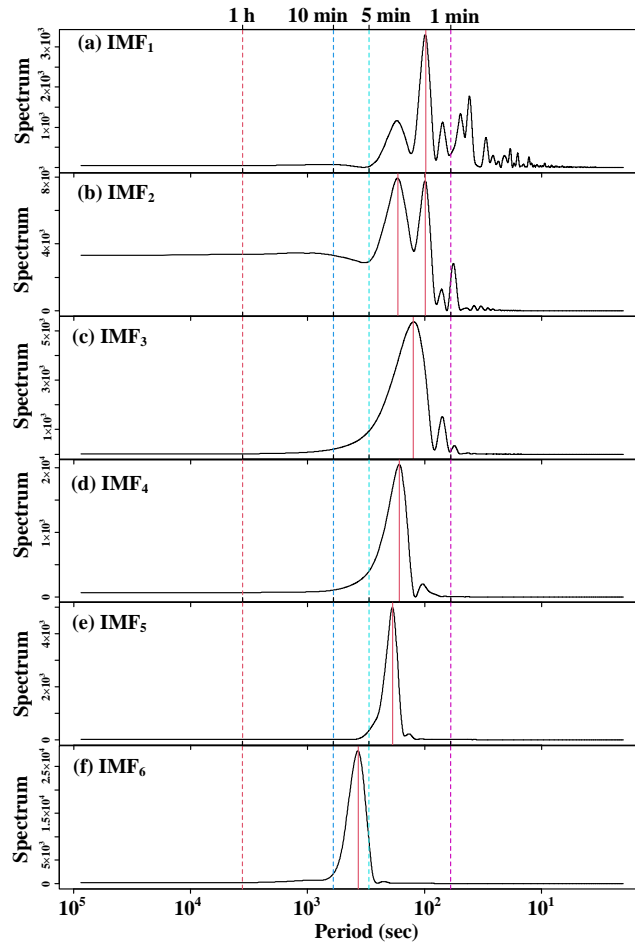
Fig. 2 Power spectral density of the intrinsic mode function (IMF) of above-canopy CO_2 concentrations in the Mongolian oak forest on July 2, 2020 (24 h).

To examine the spatio-temporal variations in large eddies, this study compared the A_m and P_m values above canopies across different forest stands. The analysis utilized data from daytime, nighttime, and transition periods in both the growing and dormant seasons. The averages of A_m and P_m averages for the above-canopy $[CO_2]$ in the three forest stands ranged from 1.588 to 136.667 ppm and from 2.313 to 2.784 min, respectively (Table 2). Fig. 3 demonstrated significant seasonal and diurnal differences ($P < 0.01$) in P_m, with higher values during daytime in the growing season, and lower values during the daytime in the dormant season. Moreover, P_m was significantly different ($P < 0.01$) among different forest stands during the same time period, with

MBF stand having the highest values, followed by the MOF, and the lowest values in the LPF. During the growing season, the A_m values were significantly higher than those during the dormant season, with both daytime and nighttime values also exhibiting significant differences ($P < 0.01$) among different forest stands. This observation provided evidence of significant spatio-temporal variability in large eddies influenced by gusts.

Table 2 Mean of the A_m in ppm and P_m in second (s) for three forest stands at different periods

Variable	Tower site	Growing season			Dormant season		
		DT[1]	NT[2]	TP[3]	DT	NT	TP
A_m[4] (ppm)	MBF[6]	57.932	**139.667**	136.717	2.219	5.212	4.944
	MOF[7]	36.160	57.945	55.777	2.699	5.175	4.637
	LPF[8]	52.688	58.816	60.147	**1.588**	2.985	2.456
P_m[5] (s)	MBF	154.563	**167.024**	164.824	158.449	151.428	158.121
	MOF	151.986	160.633	159.146	153.091	147.491	153.274
	LPF	149.003	143.950	145.696	143.458	**138.794**	142.009

[1] DT represents daytime; [2] NT represents nighttime; [3] TP represents transition period. [4] A_m represents the maximum amplitude of short-term CO_2 concentration fluctuations; [5] P_m represents the corresponding period of maximum amplitude. [6] MBF represents mixed broad-leaved forest; [7] MOF represents Mongolian oak forest; [8] LPF represents Larch plantation forest.

To estimate the uncertainty of F_s using an individual tower, a comprehensive analysis of its diurnal and seasonal dynamics, as well as the functional relationship between F_s and u_*, was necessary. Significant diurnal variations and seasonal differences in F_s were observed across the three forest stands, as shown in Fig. 4. During the growing season, the median diurnal variation of F_s for the three forest stands ranged from −2.960 to 2.647 μmol m^{-2} s^{-1}, whereas during the dormant season, it ranged from

317   −1.306 to 1.012 μmol m^{-2} s^{-1}. Comparing the extent of F$_s$ diurnal variation among the

318   three forest stands, MBF exhibited the largest extent during the growing season, while

319   the extent of the three forest stands were similar during the dormant season. Notably, it

320   was observed that the amplitudes for longer P_m values were greater than those for

321   shorter P_m values. This observation indicated that the larger the eddies, the greater the

322   magnitude of F$_s$.
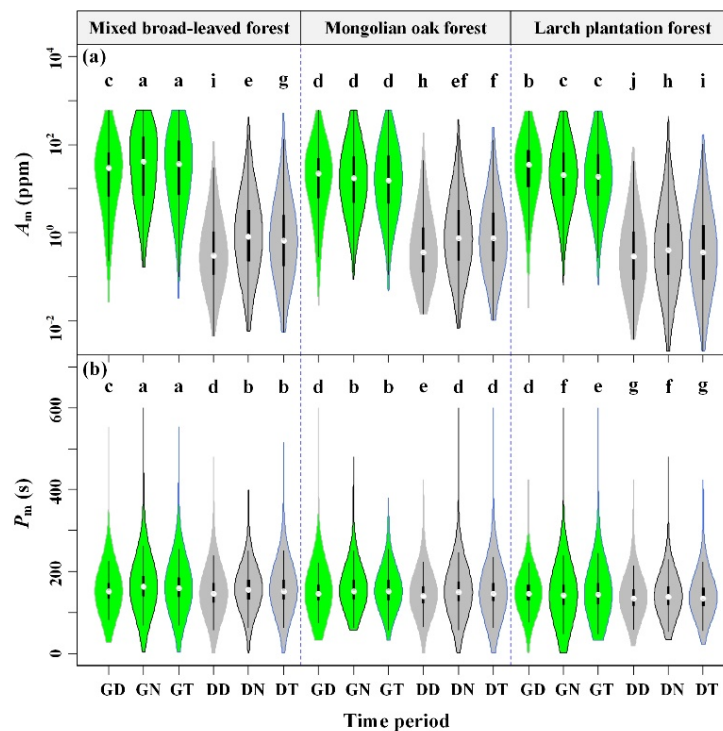
323

324   Fig. 3 Maximum amplitude (A_m) (a) and corresponding period (P_m) (b) of short-term CO_2

325   concentration fluctuations in different forest stands for seasonal and diurnal variations, where GD,

326   GN, GT, DD, DN, and DT denote the growing season daytime, growing season nighttime,

327   growing season transition period, dormant season daytime, dormant season nighttime, and

328   dormant season transition period, respectively. Columns with different lowercase letters are

329   significantly different ($P < 0.05$) according to Fisher's least significant difference test.

330   Furthermore, a u_* threshold value was identified for the variation of F$_s$ with u_*

331   during daytime in both the dormant and growing seasons (Fig. 5). When u_* fell below

332   the u_* threshold, the magnitude of F$_s$ (|F$_s$|) decreased with increasing u_*. Conversely,

333   when u_* exceeded the u_* threshold, the $|F_s|$ tended to remain relatively constant. Notably,

334   a maximum point for the $|F_s|$ was observed when the u_* was less than 0.5 m/s during the

335   growing season, whereas not during the dormant season. This phenomenon was

336   particularly evident during the nighttime and transition periods of the growing season,

337   where $|F_s|$ exhibited an initial increase followed by a subsequent decrease with u_*. These

338   observations strongly indicated that the effect of the turbulent mixing strength on the

339     $|F_s|$ over complex terrains was nonlinear and exhibited diurnal and seasonal differences.
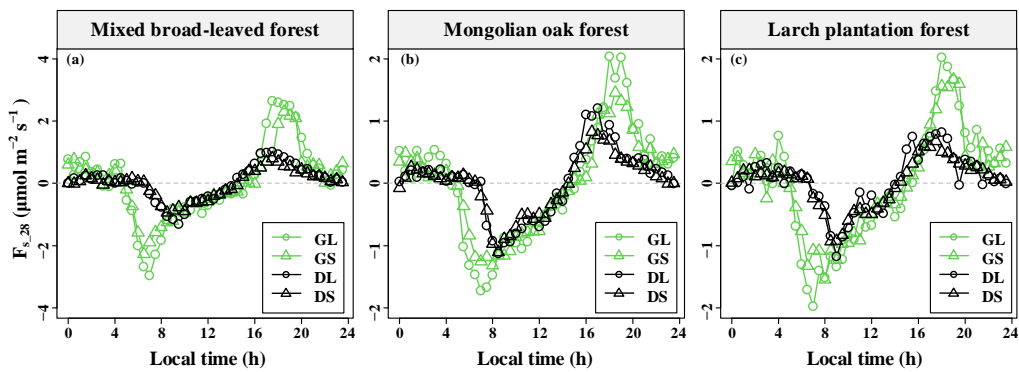
340

341   Fig. 4 Median diurnal variation of CO_2 storage flux (F_s) based on 28-min CO_2 concentration

342   averaging time windows in the three forest stands during different seasons. GS indicates the

343   growing season and a short period of maximum amplitude (P_m), GL indicates the growing season

344   and a long P_m, DS indicates the dormant season and a short P_m, and DL indicates the dormant

345   season and a long P_m.
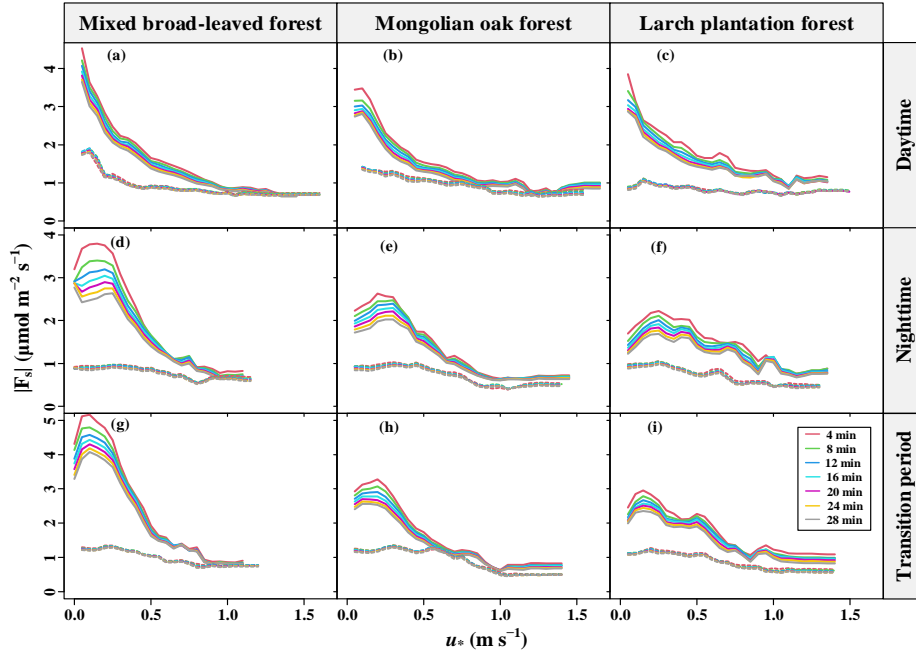
346

347   Fig. 5 Magnitudes of CO_2 storage flux ($|F_s|$) determined with different CO_2 concentration average

348   time windows as a function of the friction velocity (u_*) and moving block averages from all 30-

349   min data for the years 2020-2021. Dashed and solid lines indicate the dormant and growing

350   seasons, respectively.

351   3.2 Effect of [CO_2] fluctuations on the F_s and its uncertainty

352   To investigate the influence of the [CO_2] fluctuation periods on the error of F_s

353   measurement, this study computed the diurnal average of the standard deviation $\sigma(\varepsilon_s)$

354   of the 30-min F_s uncertainty (ε_s) separately for different P_m values and the seasons. The

355   overall distribution of ε_s showed a non-normal distribution with a high peak (kurtosis >

356   2 and $P < 0.05$, results presented in Supplementary Table 1–4). The daily variation

357   curves of $\sigma(\varepsilon_s)$ at various [CO_2] averaging time windows are presented in Fig. 6. It

358   was observed that the diurnal variation range of $\sigma(\varepsilon_s)$ was higher during the growing

359   season compared to the dormant season, regardless of the P_m lengths, indicating a

360   seasonal difference independent of the P_m. Additionally, during the growing season,

361   both MBF and MOF demonstrated evident diurnal variation in $\sigma(\varepsilon_s)$, with the peak

362   occurring at night and the trough during the daytime. The diurnal variation range of

363    $\sigma(\varepsilon_s)$ varied across the three forest stands, with MBF exhibiting the largest amplitude.

364   Furthermore, a significantly positive correlation was observed between $\sigma(\varepsilon_s)$ the

365    $|F_s|$ ($P < 0.01$), with site, seasonal, and diurnal differences (Fig. 7). The relationship

366   between $\sigma(\varepsilon_s)$ the $|F_s|$ was characterized by intercepts and slopes ranging from 1.99

367   to 2.82 µmol m^{-2} s^{-1} and from 0.24 to 0.28, respectively (results presented in the

368   Supplementary Tables 5–6). Both decreased as the $[CO_2]$ averaging time window

369   increased, with the growing season exhibiting larger values compared to the dormant

370   season (results shown in the Supplementary Tables 5–6). These findings suggested that

371   increasing the $[CO_2]$ averaging time window, results in a reduction of the random error

372   in F_s and the correlation coefficient between $\sigma(\varepsilon_s)$ and $|F_s|$. This indicated a decrease

373   in variability of $\sigma(\varepsilon_s)$ and a behavior similar to white noise.

374   To assess the impact of $[CO_2]$ fluctuations on the error and bias of F_s measurement,

375   this study compared the NRMSE and slopes of F_s based on different $[CO_2]$ averaging

376   time windows, with reference to the baseline F_{s_28}, across various P_m values, time

377   periods, and sites. As shown in Fig. 8, the NRMSE decreased and approached

378   convergence as the $[CO_2]$ averaging time windows increased. During both daytime and

379   nighttime in the growing season, the NRMSE corresponding to longer P_m was greater

380   than that corresponding to shorter P_m, while the opposite trend was observed during the

381   dormant season. Additionally, the longer the $[CO_2]$ averaging time window, the greater

382   the relative underestimation of F_s.

383
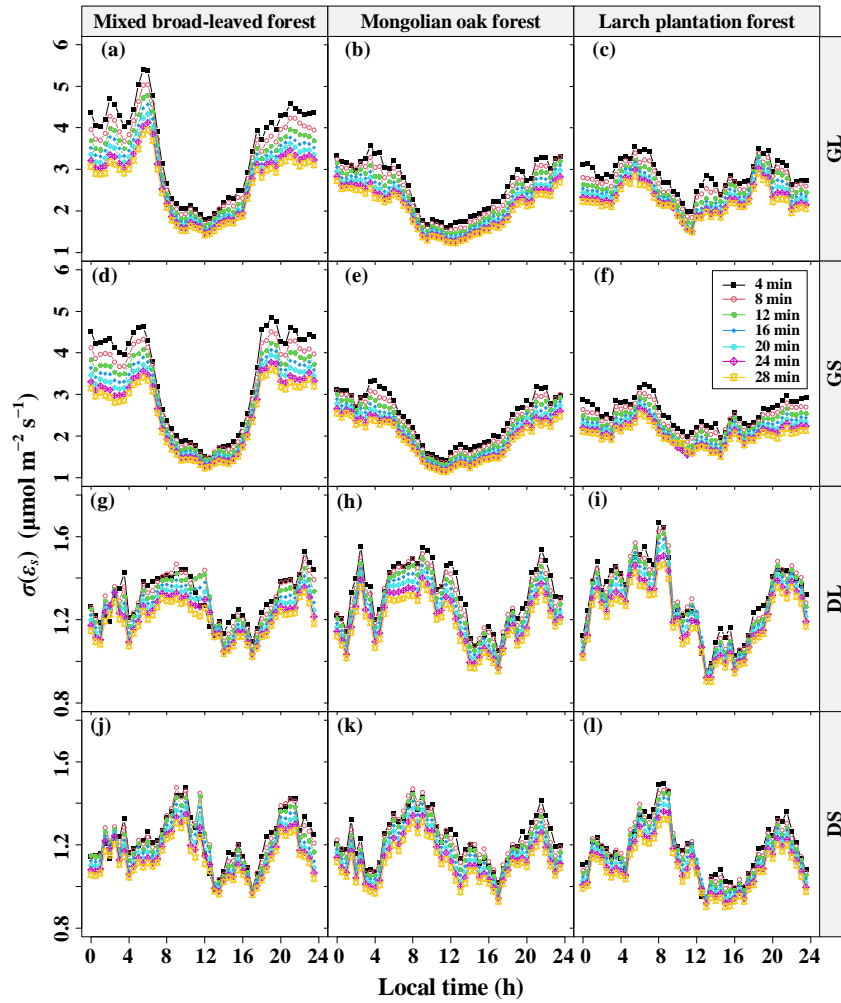
Fig. 6 Diurnal variations in the random uncertainty ($\sigma(\varepsilon_s)$) of CO_2 storage flux (F_s) errors (ε_s) at

different CO_2 concentration ([CO_2]) averaging time windows and their seasonal differences, where

GS indicates the growing season and a short period of maximum amplitude (P_m) of [CO_2]

fluctuations, GL indicates the growing season and a long P_m, DS indicates the dormant season and

a short P_m, and DL indicates the dormant season and a long P_m.
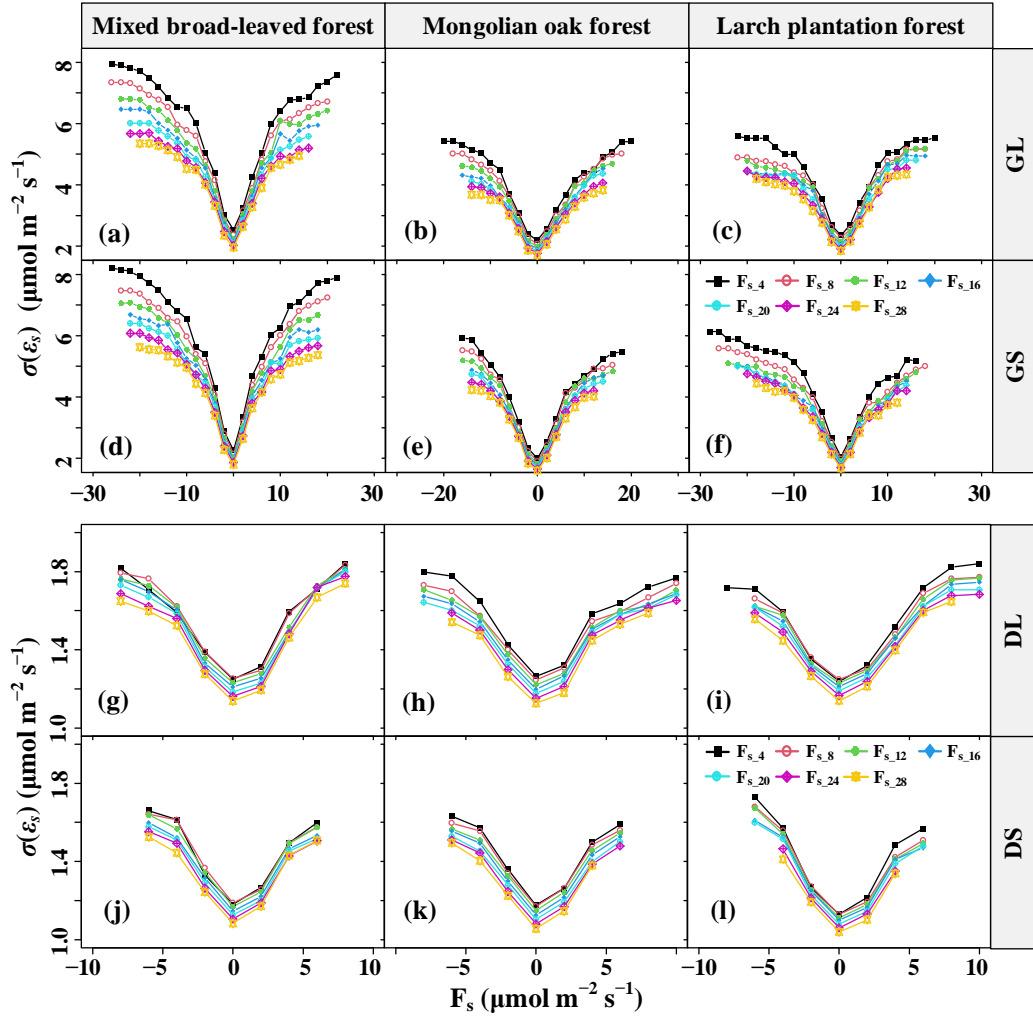
Fig. 7 Random uncertainty $\sigma(\varepsilon_s)$ of CO_2 storage flux (F_s) errors (ε_s) at different CO_2 concentration ($[CO_2]$) averaging time windows as a function of the F_s magnitude for mixed broad-leaved forest, Mongolian oak forest, and Larch plantation forest during the growing and dormant seasons. GS indicates the growing season and a short period of maximum amplitude (P_m) of $[CO_2]$ fluctuations, GL indicates the growing season and a long P_m, DS indicates the dormant season and a short P_m, and DL indicates the dormant season and a long P_m.
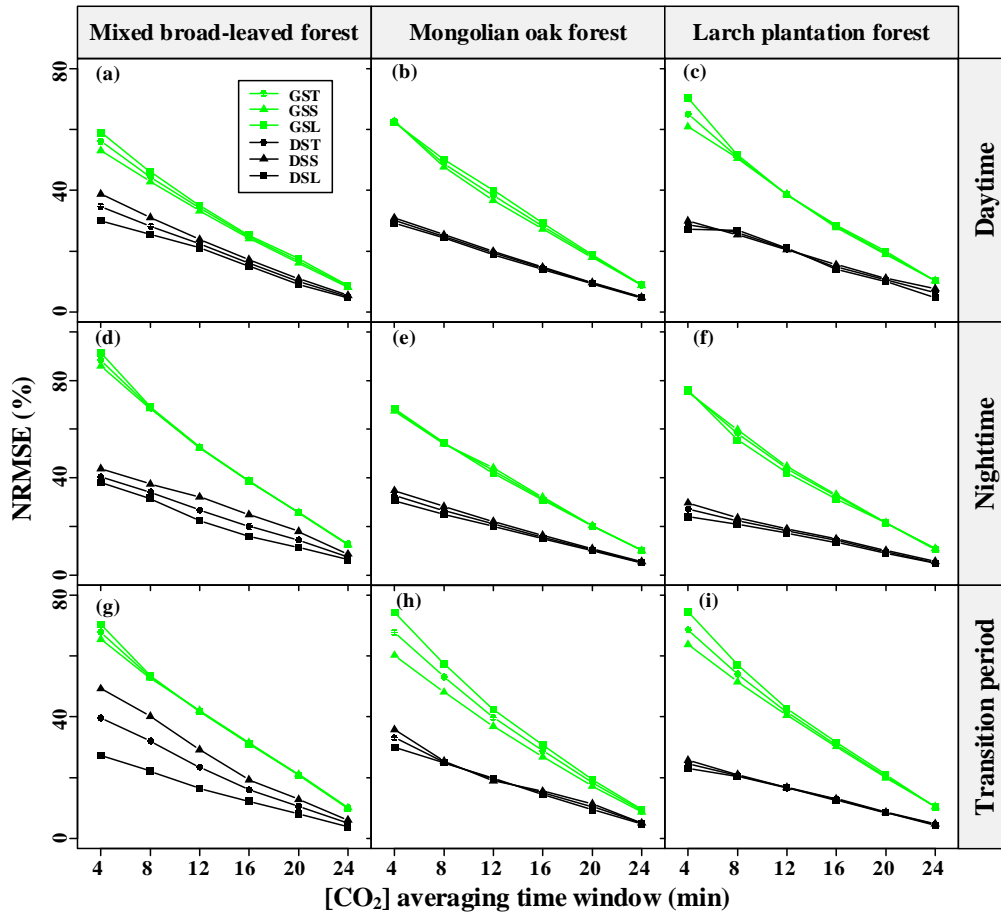
Fig. 8 Seasonal and diurnal differences in the normalized root mean square error (NRMSE) of CO_2 storage flux (F_s) versus the respective F_{s_28} values for different CO_2 concentration ($[CO_2]$) averaging time windows. GST indicates the growing season and does not distinguish the period of maximum amplitude (P_m) of $[CO_2]$ fluctuations, GSS indicates the growing season and a short P_m, GSL indicates the growing season and a long P_m, DST indicates the dormant season and does not distinguish P_m, DSS indicates the dormant season and a short P_m, and DSL indicates the dormant season and a long P_m.

The comparison of slopes between F_{s_4} and F_{s_28} in the three forest stands revealed interesting patterns, as depicted in Fig. 9. During the growing season, the slopes corresponding to the shorter P_m of $[CO_2]$ fluctuations were consistently lower than those for the longer P_m, indicating that the effect of P_m on F_s uncertainty decreased with increasing $[CO_2]$ averaging time windows. However, for the MBF stand (Fig. 9d and Fig. 9g), the slopes corresponding to the shorter P_m of $[CO_2]$ fluctuations during the dormant season nighttime were actually greater than those for the longer P_m, primarily

411   due to diurnal variations in the daily dynamics of F_s. Overall, the influence of P_m on F_s

412   uncertainty decreased with increasing [CO_2] averaging time windows. This suggested

413   that averaging [CO_2] reduced the effect of gusts on the random uncertainty in estimating

414   F_s, but led to a systematic underestimation of F_s.

415
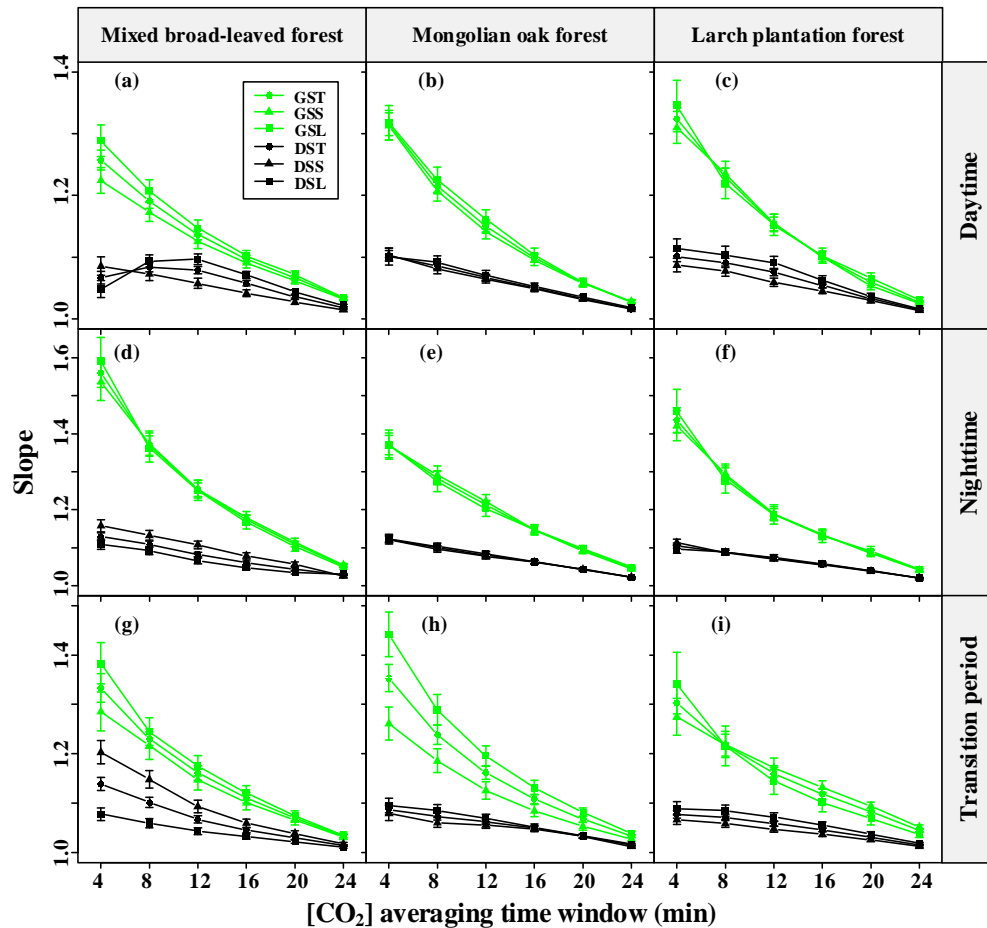
Fig. 9 Seasonal and diurnal differences in the slope of CO_2 storage flux (F_s) versus the F_{s_28} for the

different CO_2 concentration ([CO_2]) averaging time windows. GST indicates the growing season

and does not distinguish the period of maximum amplitude (P_m) cases, GSS indicates the growing

season and a short P_m, GSL indicates the growing season and a long P_m, DST indicates the

dormant season and does not distinguish P_m, DSS indicates the dormant season and a short P_m,

and DSL indicates the dormant season and a long P_m.

422   To analyze the effect of [CO_2] fluctuations on |F_s| in complex terrains, this study

423   developed a multiple linear regression model, considering the interaction effects of

424   turbulent mixing and terrain complexity on |F_s|, as shown in Fig. 10. A_m exhibited a

significant positive correlation with |F_s| in all time periods ($P < 0.05$). Conversely, P_m showed a significant negative correlation with |F_s| during the dormant season daytime, the growing season daytime, and the transition periods ($P < 0.05$). Additionally, their correlation coefficient decreased with increasing τ. In Fig. 10d and Fig. 10e, a u_* threshold was observed during the growing season nighttime. When the u_* was below the threshold, higher TCI values resulted in smaller |F_s|; whereas when the u_* was above the threshold, higher TCI values led to larger |F_s|. During the growing season nighttime and transition periods, u_* showed a significant negative correlation ($P < 0.05$) with |F_s|, and the correlation coefficient decreased with increasing TCI values. These observations suggested that the effect of turbulent mixing on the |F_s| uncertainty was regulated by terrain complexity.

A multiple linear regression model was used to analyze the effect of [CO_2] fluctuations on the random uncertainty of F_s, $\sigma(\varepsilon_s)$, in complex terrains. This model considered the interaction effects of [CO_2] fluctuations and terrain complexity on $\sigma(\varepsilon_s)$, as shown in Fig. 11. As evident from Fig. 11a and Fig. 11e, the A_m exhibited a significant positive correlation ($P < 0.05$) with $\sigma(\varepsilon_s)$ during both the dormant season's nighttime and the growing season. Throughout the transition period of the growing season, P_m displayed a significant negative correlation with $\sigma(\varepsilon_s)$ ($P < 0.05$). The magnitude of these correlation coefficients decreased with the increasing [CO_2] averaging time windows. During the transition period of the dormant season, a TCI threshold was observed, with P_m showing a significant positive correlation ($P < 0.05$) with $\sigma(\varepsilon_s)$ when the TCI was below the threshold, and a significantly negative

447 correlation ($P < 0.05$) with $\sigma(\varepsilon_s)$ when the TCI exceeded the threshold (Fig. 11b and

448 Fig. 11f). The u_* showed a significantly negative correlation with $\sigma(\varepsilon_s)$ during the

449 daytime and transition periods of the growing season ($P < 0.05$), while in other time

450 periods, u_* was significantly positively correlated with $\sigma(\varepsilon_s)$ ($P < 0.05$). The $|F_s|$

451 demonstrated a significant positive correlation with $\sigma(\varepsilon_s)$ ($P < 0.05$) in all time

452 periods, with its correlation coefficient being greater during the growing season than

453 during the dormant season. These observations suggested that the relationship between

454 the random uncertainty in F_s and [CO_2] fluctuations was moderated by topographic

455 complexity. Increasing the [CO_2] averaging time window reduced the effect of [CO_2]

456 fluctuations on the random uncertainty in F_s.
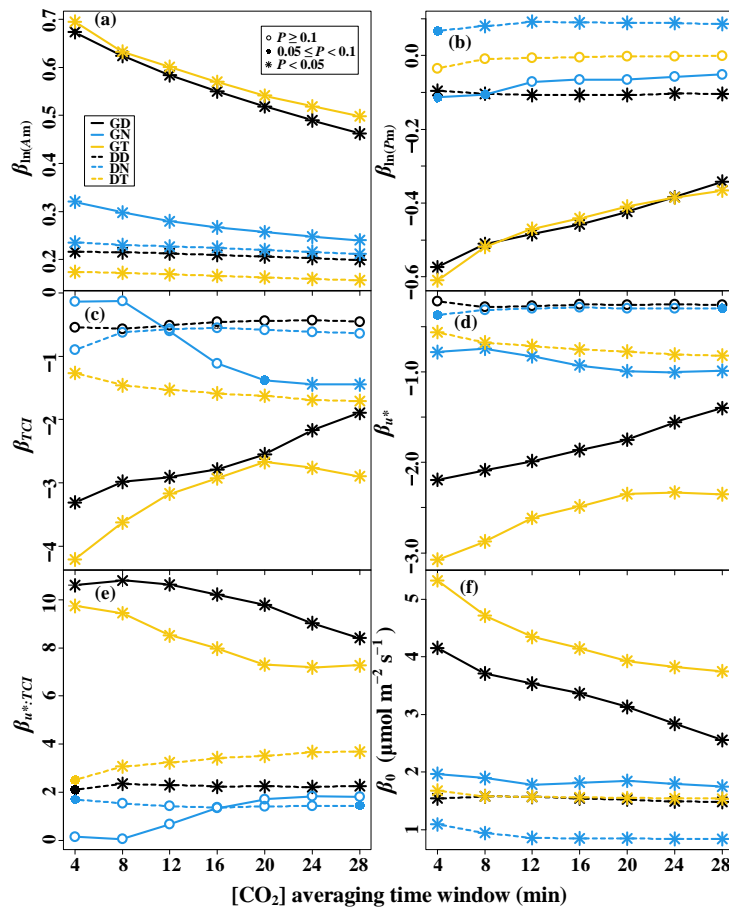
457

458   Fig. 10 Linear regression coefficients of the CO_2 storage flux (F_s) magnitude—driving factors

relationships for the seven CO_2 concentration ($[CO_2]$) averaging time windows. The predictors of the multiple linear models are (a) the logarithm of maximum amplitude of $[CO_2]$ fluctuations ($\ln(A_m)$), (b) the logarithm of the corresponding period of maximum amplitude ($\ln(P_m)$), (c) the terrain complexity index (TCI), (d) the friction velocity (u_*), and (e) the interaction term of TCI and u_*, respectively. (f) β_0 represents the intercept term.
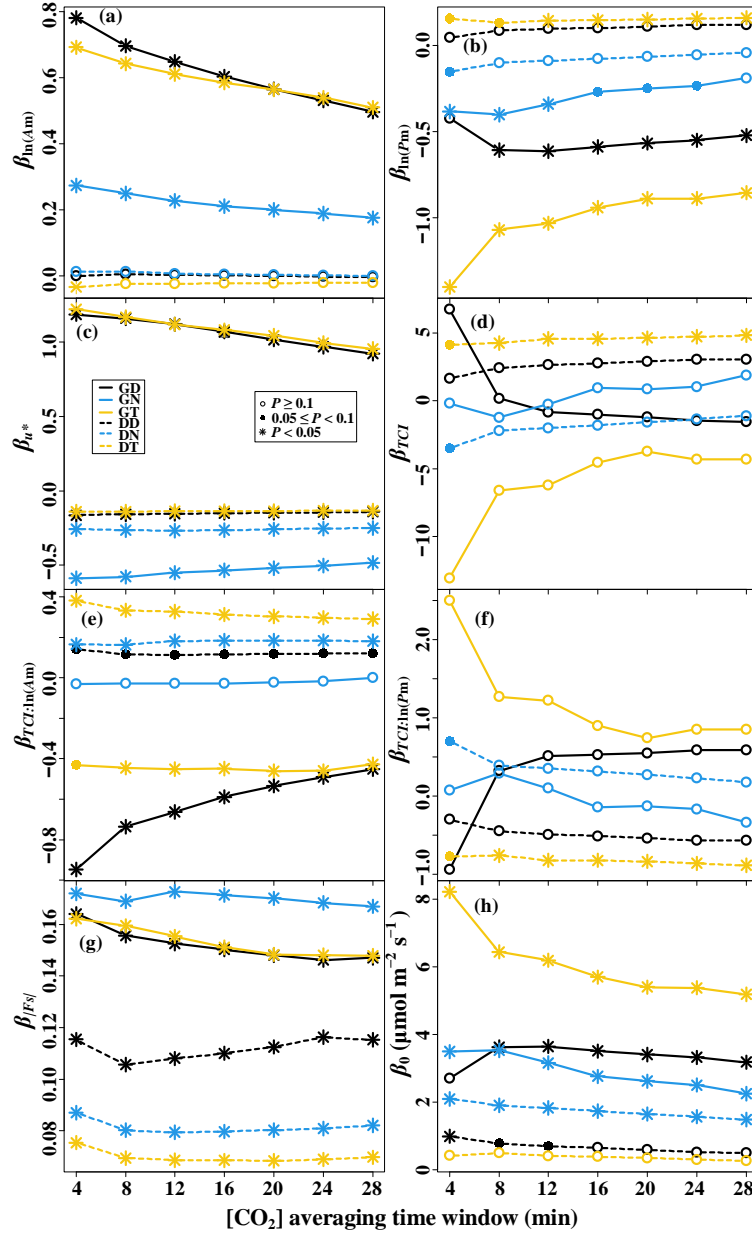
Fig. 11 Linear regression coefficients of the random uncertainty of CO_2 storage flux ($\sigma(\varepsilon_s)$)—driving factors relationships determined with Eq. (11) for the seven CO_2 concentration ($[CO_2]$) averaging time windows. The predictors of the multiple linear models are (a) the logarithm of maximum amplitude of $[CO_2]$ fluctuations ($\ln(A_m)$), (b) the logarithm of the corresponding period of maximum amplitude ($\ln(P_m)$), (c) the terrain complexity index (TCI), (d) the friction velocity (u_*)

470   (u_*), (e) the interaction term of TCI and $\ln(A_m)$, (f) the interaction term of TCI and $\ln(P_m)$, and the

471   magnitude of storage flux ($|F_s|$), respectively. (h) The intercept term is represented by β_0.

3.3 Effect of CO_2 storage fluxes uncertainty on NEE observations

The 30-min F_{s_comb} was obtained by weighing the bias and random error of F_s using different [CO_2] averaging time windows and P_m values. This study then focused on the magnitude of F_{s_comb} in relation to the F_c magnitude and its diurnal, seasonal, and site variations. To assess the significance of F_s in NEE observations, the relative contribution ratio of F_{s_comb} magnitude ($|F_{s\_comb}|/(|F_c|+|F_{s\_comb}|)$) was employed. The $|F_{s\_comb}|/(|F_c|+|F_{s\_comb}|)$ showed a decreasing trend to convergence with increasing u_* (Fig. 12). On average, the $|F_{s\_comb}|/(|F_c|+|F_{s\_comb}|)$ ranged from 17.2% to 82.0%, with a higher value during the dormant season compared to the growing season. This indicated that as turbulence intensity increased, the contribution of F_s to the NEE in forests decreased to a constant value. Nevertheless, even under strong turbulence intensity, F_s still played a significant role in the NEE observations of forests in complex terrains.
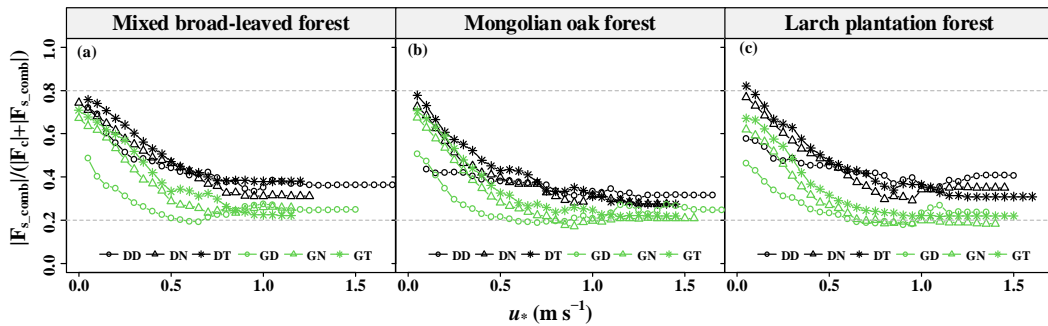
Fig. 12 Relative contribution ratio of the CO_2 storage flux magnitude ($|F_{s\_comb}|/(|F_c|+|F_{s\_comb}|)$) determined by decision-level fusion model as a function of the friction velocity (u_*) moving block averages from all 30-min data for the years 2020–2021. GD represents the growing season's daytime; GN represents the growing season's nighttime; GT represents the growing season's transition period; DD represents the dormant season's daytime; DN represents the dormant season's nighttime; DT represents the dormant season's transition period.

As indicated in Table 3, both P_m and TCI exhibited a significant positive

correct with $|F_{s\_comb}|/(|F_c|+|F_{s\_comb}|)$ ($P < 0.05$), while both A_m and u_* showed a

significant negative correlation with $|F_{s\_comb}|/(|F_c|+|F_{s\_comb}|)$ ($P < 0.05$). Notably,

seasonal variations in correlation coefficients were observed. The correlation between

the u_* and $|F_{s\_comb}|/(|F_c|+|F_{s\_comb}|)$ was more pronounced during both the dormant

season's transition period and the growing season, and it decreased with increasing TCI

values during the dormant season's daytime and nighttime.

Table 3 Linear regression coefficients of the relative contribution ratio of F_{s_comb}
magnitudes to NEE observations ($|F_{s\_comb}|/(|F_c|+|F_{s\_comb}|)$) —driving factors
relationships for the six time periods.

Time period	β_0	$\ln(P_m)$[7]	$\ln(A_m)$[8]	u_*[9]	TCI[10]	u_*:TCI	R^2
Total	0.292	0.048	−0.037	−0.334	0.790	−1.018	0.278
	***	***	***	***	***	***	***
GD[1]	0.299	0.016	−0.041	−0.183	−0.293	0.239	0.158
	***		***	***	*		***
GN[2]	0.370	0.029	−0.023	−0.386	−0.038	0.081	0.103
	***		***	***			***
GT[3]	0.161	0.060	−0.014	−0.182	1.056	−1.754	0.186
		***	***		***		***
DD[4]	0.393	0.011	−0.020	−0.154	0.306	−0.153	0.040
	***		***	*			***
DN[5]	0.661	0.012	−0.026	−0.443	−0.035	0.399	0.088
	***		***	***			***
DT[6]	0.495	0.017	−0.036	−0.294	0.564	−0.852	0.149
	***		***	***			***

[1] GD represents the growing season's daytime; [2] GN represents the growing season's nighttime;
[3] GT represents the growing season's transition period; [4] DD represents the dormant season's
daytime; [5] DN represents the dormant season's nighttime; [6] DT represents the dormant season's
transition period. [7] A_m: maximum amplitude; [8] P_m: corresponding period of maximum amplitude. [9]
u_*: friction velocity; [10] TCI: terrain complexity index; *** represents $P < 0.001$; ** represents $P <$
0.01; and * represents $P < 0.05$.

507   To evaluate the impact of F_{s_comb} on NEE_{obs} ($F_c + F_s$), we further evaluated the

508   slope (with intercept terms forced to zero) and NRMSE of $F_c + F_{s\_comb}$ compared to F_c

509     $+ F_{s\_28}$, as presented in Supplementary Materials Table 7 and Table 8. The F_{s_28} in the

510   three forest stands was underestimated by 28.6%–33.3% compared to the F_{s_comb}, and

511   the NRMSE of F_{s_comb} versus the F_{s_28} ranged from 59.2% to 67.2%. The NEE_{obs} with

512   F_{s_28} was underestimated by 1.9%–4.3% compared to the NEE_{obs} with F_{s_comb}. The

513   NRMSE of NEE_{obs} with the F_{s_comb} versus the F_{s_28} in the three forest stands ranged

514   from 16.0% to 25.4%. The analysis suggested that combining the F_s values based on

515   different averaging $[CO_2]$ time windows in the decision-level fusion model could

516   successfully weigh potential underestimation bias and random uncertainties.

517   The influences of F_s on the relationship between NEE observations and

518   meteorological drivers, indicated the effect of uncertainty in F_s estimates on NEE

519   observations. Our analysis showed that the correlations between NEE observations

520   derived from F_c+F_s and both photosynthetic photon flux density (PPFD) and air

521   temperature are lower compared to those obtained from F_c alone (Figure 1 and Figure

522   2 in the Supplementary Materials). Additionally, the estimated light saturated net CO_2

523   assimilation (A_{max}) is greater when NEE observations are estimated by F_s+F_c, as

524   opposed to when NEE is estimated solely by F_c. This suggests that F_s significantly

525   affects daytime NEE and can correct the estimation of A_{max} and related parameters. The

526   relationship between NEE observations and PPFD is influenced by the size of averaging

527   time window the F_s measurement. A larger averaging window results in less random

528   uncertainty in the F_s estimation, thereby increasing the correlation between NEE

529 observations and meteorological drivers, including PPFD and Ta.

530 **4 Discussion**

531 4.1 Short-term [CO_2] fluctuations above the forest canopy and F_s estimates in complex

532 terrains

533   Compared to flat and uniform underlying surface, complex terrain and

534 heterogeneous canopies modify the trajectory, speed distribution, and direction of the

535 airflow. Increased wind speeds and shifting wind directions also increase turbulent

536 activity above the canopy, facilitating the mixing and dispersion of CO_2. This study

537 found that short-term fluctuations of [CO_2] above the canopy exhibited a range of 1 to

538 10 min (Fig. 2). These fluctuations were characterized by an average P_m ranging from

539 2.313 to 2.784 min (Table 2). Our results are in line with previous research using

540 wavelet analysis, which reported fluctuation periods of [CO_2] within and above the

541 forest canopy to be between 14 and 116 s (Cava et al., 2004). Their observations of the

542 canopy waves during periods of extreme atmospheric stability (when $z/L \gg 1$) exhibited

543 a dominant period of 1–2 min, consistent with our findings. The period of [CO_2]

544 fluctuations was found to be predominantly influenced by turbulent fluxes and the

545 residence time of CO_2 within the canopy. This indicated a potential correlation between

546 P_m and the residence time of CO_2 within the canopy. Fuentes et al. (2006) employed a

547 Lagrangian model and calculated the residence time of air parcels released near the

548 ground and canopy, finding values ranging from 3 to 10 min and from 1 to 10 min,

549 respectively. Similarly, Edburg et al. (2011) used the standard deviation of [CO_2]

averages to determine CO_2 residence time at different locations, including the ground, within the canopy, and in their gas mixtures, yielding values of 8.6, 3.6, and 5.6 min, respectively. The results of these simulation experiments are consistent with our study, further supporting the association between $[CO_2]$ fluctuations above the forest canopy and CO_2 residence time.

Tree density and canopy structure also play a role in influencing the air parcel residence time; in flat terrains, the air parcel residence time correlate with u_* (Gerken et al., 2017), and an increase in vegetation leaf area leads to longer residence times when turbulence is not fully penetrative. During the growing season, forests in our study site exhibit higher leaf area index and greater canopy densities than during the dormant season (Li et al., 2023), resulting in longer P_m of short-term $[CO_2]$ fluctuations above the canopy (Fig. 3). Additionally, at night, stable atmospheric conditions lead to longer residence times due to suppressed turbulent mixing, resulting in relatively long nighttime P_m values compared to daytime and transition periods (Fig. 3).

Complex terrains introduce complex changes in air flow structures, including gravity-induced waves, drainage, and nonlinear waves induced by single gusts, leading to dramatic $[CO_2]$ fluctuations. These dynamics contribute to uncertainties in estimating F_s. During night, the difference between incoming and outgoing longwave radiation over the valley soil surface and vegetation canopy gives rise to radiative cooling. Subsequently, the air near the soil surface experiences a gravity-induced downslope acceleration, potentially causing katabatic flow. As inertia-driven upslope winds are halted by katabatic acceleration, a local shallow drainage flow is established, reaching

a quasi-equilibrium state approximately 1.5 h after sunset (Nadeau et al., 2013). Under

stable atmospheric conditions, even gentle slopes (around 1°) can generate strong

gravity-driven waves (Belušić and Mahrt, 2012). Consequently, advection may

complicate the interpretation of nighttime EC measurements at certain relatively gentle

sites, but this complexity is not evident during daytime measurements (Leuning et al.,

2008). Advection plays a role in depleting the CO_2 accumulated within the canopy,

resulting in lower F_s fluxes and establishing an inverse relationship between storage

and advection (Van Gorsel et al., 2011). The occurrence of larger F_s values for long P_m

values suggests weaker advection compared to short P_m values (Fig. 4). In our study,

we observed that the F_s magnitude was relatively large during nighttime and transition

periods, while it was smaller during daytime (Fig. 4), which is consistent with the

findings reported by Wang et al. (2016).

The terrain unevenness and the complexity of canopy structure significantly affect the airflow divergence in the atmospheric boundary layer. This results in weakened air

circulation within the canopy and spatial variation in the patterns and extent of airflow

separation (Grant et al., 2015). During nighttime and transition periods in a closed

canopy, the turbulent coupling state above and below the canopy gradually decouples,

eventually reaching complete decoupling as the u_* decreases (Fig. 5). However, this

decoupling does not lead to stable stratification within the canopy. Despite the

occurrence of decoupling and advection in the closed canopy, waves are unlikely to

exist within the canopy itself (Van Gorsel et al., 2011). As a result, a consistent trend

in the variation of F_s with τ is observed across the three forest stands during the growing

season, independent of P_m (Fig. 9). Conversely, in an open canopy where waves are

present, the observations of F_s become more complex. This complexity could be the

primary reason why the variation of F_s with $[CO_2]$ averaging time windows differs

between the three forest stands for short P_m values during the dormant season daytime

(Fig. 9). The presence of waves introduces additional variability in the measurements,

leading to differences in F_s estimates based on different $[CO_2]$ averaging time windows

in these particular conditions.

4.2 Uncertainty in forest ecosystem F_s measurement in complex terrains

The random uncertainty of F_s shares similarities with NEE estimation. For

example, the magnitude of F_s measurements is positively correlated with the standard

deviation of random uncertainty in F_s. Additionally, the overall distribution of F_s

measurements exhibits a non-Gaussian distribution with a high peak, aligning with the

statistical properties of NEE uncertainty (Richardson et al., 2006; Richardson et al.,

2008). The uncertainty in the storage term depends a lot on the set-up used, together

with the biological activity of the ecosystem, and the height of the control volume. In

addition, various factors contribute to the uncertainty in F_s estimates, including flux

measurement footprint variations, sampling frequency, spatial sampling resolution of

CO_2/H_2O concentrations, and instrumental measurement accuracy. The accuracy and

precision requested for the CO_2 and H_2O concentration measurements are ± 1 µmol

mol^{-1} and ± 1 mmol mol^{-1}, respectively (Montagnani et al., 2018). The uncertainty

arising from variations in the flux measurement footprint is considerable, typically on

the order of tens of percentages, which is an order of magnitude higher than typical

616   sensor errors (Metzger, 2018). The AP200 adopts buffer volumes to mix the gas. The

617   LI-850 analyzer integrated within in AP200 exhibits a sensitivity to water vapor of less

618   than 0.1 μmol CO_2 per mmol mol^{-1} H_2O, and a sensitivity to CO_2 of less than 0.0001

619   mmol mol^{-1} H_2O per μmol CO_2. Efforts to reduce random errors in [CO_2] originating

620   from pressure fluctuations include adding buffer volumes before IRGA pumping tests

621   (Marcolla et al., 2014). The buffer volumes are fully mixed during gas extraction and

622   performs a weighted average of [CO_2] instantaneous measurements to minimize the

623   sampling error for each level's [CO_2] measurement (Cescatti et al., 2016).

624   The F_s estimates can be influenced by singular eddies that penetrate inside the

625   canopy (Finnigan, 2006). Accurate calculation of F_s requires considering the period of

626   [CO_2] fluctuations with the eddy coherence structure. The spectral energy of the F_s time

627   series is primarily concentrated between 0.001 and 0.2 Hz (500 and 5 s, respectively).

628   However, even with sampling frequencies of 2 Hz and below, significantly lower F_s

629   values are obtained (Bjorkegren et al., 2015). The Nyquist-Shannon sampling theorem

630   dictates that accurate measurements of [CO_2] require a sampling period no longer than

631   half the period of [CO_2] fluctuations. Consequently, to monitor short-term changes in

632   [CO_2], measurements must be taken over a period no longer than half of the period

633   corresponding to the maximum amplitude (or major energy) of [CO_2] fluctuations. In

634   this study, the average P_m for [CO_2] fluctuations fell within the range of 2.313–2.784

635   min (Table 2). Therefore, it is crucial to ensure that the sampling period for [CO_2] does

636   not exceed 1.256 to 1.392 min, which corresponds to half the average P_m range.

637   Monitoring fluctuations of P_m for less than 4 min during a 2-min monitoring period of

638 [CO$_2$] presents a significant challenge. This is a primary reason that the systematic bias

639 and random error in F$_s$ estimate with a single profile system are irreconcilable (Wang

640 et al., 2016). Short-term [CO$_2$] fluctuations are mainly influenced by boundary layer

641 turbulence, and sampling errors in incomplete fluctuation cycles will be superimposed

642 with the real advection flux (anisotropy) dispersion in complex terrains (Van Gorsel et

643 al., 2011). This substantially increases the random uncertainty in F$_s$ based on shorter

644 [CO$_2$] averaging time windows (Fig. 6 and Fig. 8). As a result, the deviation of NEE

645 estimates from the actual value expands.

646   Fluxes in heterogeneous regions are significantly higher than in uniform regions.

647 The energy transfer from the ground surface to large eddies occurs primarily in areas

648 with pronounced heterogeneity, and this energy distribution is uneven across the region

649 (Aubinet et al., 2012). Once large-scale eddies acquire energy, their cascading of energy

650 to smaller-scale eddies is influenced by topographic features, leading to variations in

651 these smaller-scale eddies along different flow streams (Chen et al., 2023). In complex

652 terrains, the bidirectional airflow within forests along slopes can cause the decoupling

653 of soil CO$_2$ fluxes from EC measurements above the forest canopy (Feigenwinter et al.,

654 2008; Aubinet et al., 2003), leading to significant errors in CO$_2$ flux measurements.

655 Forest soil serves as the primary source of CO$_2$ gas and regions of high flux over

656 complex terrains act like chimneys, transporting air parcels from the soil surface within

657 forests (Chen et al., 2019). By increasing the number of gas concentration sampling

658 points near the ground, the horizontal representativeness can be enhanced, thereby

659 reducing the bias in the estimation of F$_s$ (Nicolini et al., 2018). In situations where

660 turbulence is not well-developed, and CO_2 mixing is inadequate, the trend of F_s with

661 turbulence intensity aligns with that of advective fluxes, which is opposite to that of

662 turbulent fluxes (Mchugh et al., 2017). The temporal dynamics and amplitudes of F_s

663 changes are influenced by topography complexity and wind conditions above the forest

664 canopy (Fig. 10). Locations with more complex and sloping topography at the flux

665 tower are more likely to generate advective fluxes that may not be easily observed at a

666 single point.

667   Estimating landscape CO_2 fluxes in complex terrains solely based on

668 measurements from a single flux tower can introduce significant errors and biases that

669 are not acceptable. The magnitude of these errors in F_s estimates is dependent on the

670 height of the forest canopy and the endogenous source/sink (Chen et al., 2020). To

671 mitigate errors and biases associated with estimating F_s in complex terrains, we

672 employed a regression modeling approach using the decision-level fusion model. This

673 method involves computing a weighted average of F_s based on different $[CO_2]$

674 averaging time windows, effectively reducing errors and biases in the estimation of F_s

675 (see Table 5). In fact, from the definition of storage flux, it can be seen that weighting

676 the storage flux is essentially weighting the $[CO_2]$ in the average time window, which

677 means replacing spatial sequences with temporal sequences for weighting. The

678 weighting coefficients used to construct the model were based on the relative errors and

679 biases of F_s estimation, with the weighting coefficient decreasing as the represented

680 moment's length increased. To obtain more accurate estimates of forest ecosystem F_s in

681 complex terrains, further research should focus on understanding the spatiotemporal

682   patterns and dynamics of $[CO_2]$.

683   **5 Conclusions**

684   This study investigated the impact of short-term $[CO_2]$ fluctuations on the

685   estimation of F_s in temperate forest ecosystems within complex terrains. Additionally,

686   it examined the F_s uncertainty and the contribution of the F_s to NEE using data from

687   three flux towers. To enhance F_s uncertainty estimation, statistical sampling techniques

688   were applied based on the individual tower approach.

689   The results highlighted the significance of considering multiple time windows for

690   averaging $[CO_2]$ when estimating F_s, as $[CO_2]$ above the forest canopies exhibited

691   fluctuations with periods ranging from 1 to 10 minutes. Diurnal, seasonal, and spatial

692   variations were observed in the amplitude and periodicity of $[CO_2]$ fluctuations,

693   highlighting the need for thoughtful sampling strategies. The use of individual gas

694   analyzers to sample the CO_2 in the control volume was inadequate, leading to

695   systematic biases and random errors in the F_s estimates. Increasing $[CO_2]$ averaging

696   time windows mitigated the effect of $[CO_2]$ fluctuations on F_s estimates, reducing both

697   their magnitude and uncertainty.

698   The study also revealed that the uncertainty of F_s followed a non-normal

699   distribution, with its standard deviation positively correlated with F_s magnitude, which

700   has important implications for quality control. To improve F_s estimation, a decision-

701   level fusion model was introduced, integrating F_s estimates from multiple $[CO_2]$

702   averaging time windows, effectively reducing the impact of short-term $[CO_2]$

703 fluctuations while considering underestimation bias and random errors. The

704 contribution of F_s to NEE exhibited diurnal, seasonal, and spatial variations associated

705 with u_*, contributing to the NEE observations at rates ranging from 17.2% to 82.0%

706 depending on the turbulent mixing and terrain complexity. The influence of terrain

707 complexity on the relationship between $[CO_2]$ fluctuations, turbulent mixing, and the

708 contribution of F_s to NEE was also evident. The findings from the three flux towers

709 allowed for the generalization of these results beyond the study site. These insights

710 provide crucial scientific support for the practical application of the eddy covariance

711 technique and advance our understanding of accurately estimating NEE in forest

712 ecosystems in complex terrains.

713 **Appendix A**

714 *A.1 the weight parameters of the decision-level fusion model*

715 For each 30-min CO_2 storage flux (F_s) estimate based on the CO_2 concentration

716 ($[CO_2]$) averaging time window (τ), the weight in the decision-level fusion model can

717 be obtained by weighting the random uncertainty and bias of F_{s_τ}.

718 The weight of the random uncertainty for the F_{s_τ} is expressed as follows:

$$w_\tau = \frac{1/\sigma(\varepsilon_\tau)}{\sum_j 1/\sigma(\varepsilon_j)}, \tag{A.1}$$

719 where $\sigma(\varepsilon_\tau)$ is the random uncertainty of the F_{s_τ}, qualified as the standard deviation.

720 The weight of the bias for the F_{s_τ} is expressed as follows:

$$W_\tau = \frac{K_\tau}{\sum_j K_j}, \tag{A.2}$$

721 where K_τ is the slope between the F_{s_τ} and F_{s_28}.

722 Ultimately, the weight of the F_{s_τ} in the decision-level fusion model can be

723   calculated using the following equation:

$$w_\tau^* = rw_\tau + (1-r)W_\tau, \tag{A.3}$$

724   where r represents the proportion of the weight of random uncertainty.

725   *A.2 Complex terrain index*

726   This study employed a novel descriptor called the terrain complexity index (*TCI*)

727   to quantify the complexity of the three-dimensional terrain. For a given unit area, the

728   *TCI* equation can be expressed as follows:

$$TCI = (1 - P_d\cos\alpha_d)(1 - Z_d^{-1})(D_f - 2)^{-H/\ln(12)}, \tag{A.4}$$

729   where, P_d represents the volume of terrain above the lowest elevation of an area

730   unit (V_u) divided by the product of its largest vertically projected area (S_v) and the

731   edge length of the side of the area unit (d), expressed as $P_d = V_u/(S_v d)$; P_d was

732   defined to be one when the S_v is zero. Given V_u, an increase in S_v correlates with a

733   higher degree of terrain complexity. Notably, the P_d is defined as 1 when the terrain

734   volume is 0 or when the terrain surface of the area unit was parallel to the horizontal

735   plane and was smooth and homogeneous. α_d indicates the slope of the area unit. Z_d

736   denoted the terrain roughness, which defined as the ratio of the terrain surface area to

737   the projected horizontal plane (Loke and Chisholm, 2022). The value of Z_d is in the

738   range of [1, +∞). The larger Z_d, the more complex the terrain. D_f is the fractal

739   dimension of terrain surface area, which ranged from 2 to 3 and described the

740   complexity in spatially self-similar structure of the local surface within the area unit

741   and the area unit surface (B. B. Mandelbrot, 1967; Taud and Parrot, 2005). Employing

742   terrain surface area, the box-counting method is used to estimate fractal dimension of

743 unit area. *H* represented the Shannon-Wiener index and expressed as $H =$

744 $-\sum_{i=1}^{n} P_i \ln(P_i)$, capturing the uniformity of the spatial distribution of the pixel

745 aspects within the area unit (Brown, 1997). When the aspect of each pixel is divided

746 into 30° segments, P_i denotes the proportion of the ith type of pixel aspects within the

747 area unit and *n* was the total number of pixel aspect types within the area unit. A

748 larger *H* indicates a more complex terrain. When the number of pixel aspect types in

749 the area unit is kept constant, it's essential to recognize that greater uniformity in the

750 distribution of all pixel aspect in the area unit results in a larger *H*. Similarly, when the

751 uniformity of the distribution of pixel aspects in the area unit is kept constant, a larger

752 *H* is achieved with an increase in the observation of the number of pixel aspect types.

753   To quantify the terrain complexity of the underlying surface around the flux towers,

754 we computed the quartiles of *TCI* for all area units within a sector (divided by 30°) with

755 a radius of 380 m. A weighted geometric mean was employed to construct *TCIs*, which

756 describe the statistical distribution of *TCI* of the sector. The *TCIs* represents the

757 topographic complexity of the sector and are calculated using the following equation:

758 $$TCI_s = (TCI_5 TCI_{25} TCI_{50} TCI_{75} TCI_{95})^{1/5} \qquad (A.5)$$

759 where *TCI$_5$*, *TCI$_{25}$*, *TCI$_{50}$*, *TCI$_{75}$*, and *TCI$_{95}$* are the quartiles of 5%, 25%, 50%, 75%,

760 and 95%, respectively. The *TCIs* values range from 0 to 1, with higher values indicating

761 greater terrain complexity.

762 *Data availability.* Data used in this paper are available at the Science Data Bank

763 (https://www.scidb.cn/en/s/7ZfQZv) or upon request to the corresponding author.

764 *Author contributions.* DT developed the manuscript; JZ was responsible for

conceptualizing the idea and designing the research study; TG substantially structured

the manuscript; FY contributed to the data collection process; YZ helped in the design

and preparation of the figures and tables; XZ and BY revised the manuscript.

Competing interests. The authors declare that they have no known competing

financial interests or personal relationships that could have appeared to influence the

work reported in this paper.

Acknowledgments. We are grateful to Qingyuan Forest CERN, Chinese Academy of

Sciences/Qingyuan Forest, National Observation and Research Station, Liaoning

Province, China for providing forest sites, instrument systems, and logistic supports.

Financial support. This research was financially supported by the National Natural

Science Foundation of China (No. 32192435), the China Postdoctoral Science

Foundation (No. 2023M733672), Key R&D Program of Liaoning Province

(2023JH2/101800043), and the Postdoctoral Research Startup Foundation of Liaoning

Province of China (No. 2022-BS-022).

Reference

Aubinet, M., Heinesch, B., and Yernaux, M.: Horizontal and Vertical CO_2 Advection In A Sloping Forest, Boundary-Layer Meteorology, 108, 397-417, 10.1023/a:1024168428135, 2003.

Aubinet, M., Vesala, T., and Papale, D.: Eddy Covariance: A Practical Guide to Measurement and Data Analysis, Springer Atmospheric Sciences, Springer, Dordrecht, XXII, 438 pp., 10.1007/978-94-007-2351-1, 2012.

Aubinet, M., Grelle, A., Ibrom, A., Rannik, Ü., Moncrieff, J., Foken, T., Kowalski, A. S., Martin, P. H., Berbigier, P., Bernhofer, C., Clement, R., Elbers, J., Granier, A., Grünwald, T., Morgenstern, K., Pilegaard, K., Rebmann, C., Snijders, W., Valentini, R., and Vesala, T.: Estimates of the Annual Net Carbon and Water Exchange of Forests: The EUROFLUX Methodology, in: Advances in Ecological Research Volume 30, Advances in Ecological Research, 113-175, 10.1016/s0065-2504(08)60018-5, 2000.

B. B. Mandelbrot: How Long Is the Coast of Britain? Statistical Self-Similarity and Fractional Dimension, Science, 156, 636-638, 1967.

Belušić, D. and Mahrt, L.: Is geometry more universal than physics in atmospheric boundary layer flow?,

Journal of Geophysical Research: Atmospheres, 117, n/a-n/a, 10.1029/2011jd016987, 2012.

Bjorkegren, A. B., Grimmond, C. S. B., Kotthaus, S., and Malamud, B. D.: CO_2 emission estimation in the urban environment: Measurement of the CO_2 storage term, Atmospheric Environment, 122, 775-790, 10.1016/j.atmosenv.2015.10.012, 2015.

Brown, S.: Estimating Biomass and Biomass Change of Tropical Forests: A Primer, FAO Forestry Paper, 134, 1997.

Cava, D., Giostra, U., Siqueira, M., and Katul, G.: Organised motion and radiative perturbations in the nocturnal canopy sublayer above an even-aged pine forest, Boundary-Layer Meteorology, 112, 129-157, DOI 10.1023/B:BOUN.0000020160.28184.a0, 2004.

Cescatti, A., Marcolla, B., Goded, I., and Gruening, C.: Optimal use of buffer volumes for the measurement of atmospheric gas concentration in multi-point systems, Atmospheric Measurement Techniques, 9, 4665-4672, 10.5194/amt-9-4665-2016, 2016.

Chen, B., Chamecki, M., and Katul, G. G.: Effects of topography on in-canopy transport of gases emitted within dense forests, Quarterly Journal of the Royal Meteorological Society, 145, 2101-2114, 10.1002/qj.3546, 2019.

Chen, B. C., Chamecki, M., and Katul, G. G.: Effects of Gentle Topography on Forest-Atmosphere Gas Exchanges and Implications for Eddy-Covariance Measurements, J Geophys Res-Atmos, 125, ARTN e2020JD032581
10.1029/2020JD032581, 2020.

Chen, J., Chen, X., Jia, W., Yu, Y., and Zhao, S.: Multi-sites observation of large-scale eddy in surface layer of Loess Plateau, Science China Earth Sciences, 66, 871–881, https://doi.org/10.1007/s11430-022-1035-4, 2023.

de Araújo, A. C., J.P.H.B., O., Dolman, A. J., B., K., M.J., W., and J.R., E.: Implications of CO2 pooling on delta C13 of ecosystem respiration and leaves in Amazonian forest, Biogeosciences, 5, 779-795, 10.5194/bg-5-779-2008, 2008.

de Araújo, A. C., Dolman, A. J., Waterloo, M. J., Gash, J. H. C., Kruijt, B., Zanchi, F. B., de Lange, J. M. E., Stoevelaar, R., Manzi, A. O., Nobre, A. D., Lootens, R. N., and Backer, J.: The spatial variability of CO_2 storage and the interpretation of eddy covariance fluxes in central Amazonia, Agricultural and Forest Meteorology, 150, 226-237, 10.1016/j.agrformet.2009.11.005, 2010.

Edburg, S. L., Stock, D., Lamb, B. K., and Patton, E. G.: The Effect of the Vertical Source Distribution on Scalar Statistics within and above a Forest Canopy, Boundary-Layer Meteorology, 142, 365-382, 10.1007/s10546-011-9686-1, 2011.

Feigenwinter, C., Bernhofer, C., and Vogt, R.: The Influence of Advection on the Short Term CO_2-Budget in and Above a Forest Canopy, Boundary-Layer Meteorology, 113, 201-224, 10.1023/B:BOUN.0000039372.86053.ff, 2004.

Feigenwinter, C., Bernhofer, C., Eichelmann, U., Heinesch, B., Hertel, M., Janous, D., Kolle, O., Lagergren, F., Lindroth, A., Minerbi, S., Moderow, U., Mölder, M., Montagnani, L., Queck, R., Rebmann, C., Vestin, P., Yernaux, M., Zeri, M., Ziegler, W., and Aubinet, M.: Comparison of horizontal and vertical advective CO_2 fluxes at three forest sites, Agricultural and Forest Meteorology, 148, 12-24, 10.1016/j.agrformet.2007.08.013, 2008.

Finnigan, J.: The storage term in eddy flux calculations, Agricultural and Forest Meteorology, 136, 108-113, 10.1016/j.agrformet.2004.12.010, 2006.

Finnigan, J., Ayotte, K., Harman, I., Katul, G., Oldroyd, H., Patton, E., Poggi, D., Ross, A., and Taylor, P.: Boundary-Layer Flow Over Complex Topography, Boundary-Layer Meteorology, 177, 247-313,

10.1007/s10546-020-00564-3, 2020.

Fuentes, J. D., Wang, D., Bowling, D. R., Potosnak, M., Monson, R. K., Goliff, W. S., and Stockwell, W. R.: Biogenic Hydrocarbon Chemistry within and Above a Mixed Deciduous Forest, Journal of Atmospheric Chemistry, 56, 165-185, 10.1007/s10874-006-9048-4, 2006.

Gao, T., Yu, L.-Z., Yu, F.-Y., Wang, X.-C., Yang, K., Lu, D.-L., Li, X.-F., Yan, Q.-L., Sun, Y.-R., Liu, L.-F., Xu, S., Zhen, X.-J., Ni, Z.-D., Zhang, J.-X., Wang, G.-F., Wei, X.-H., Zhou, X.-H., and Zhu, J.-J.: Functions and applications of Multi-Tower Platform of Qingyuan Forest Ecosystem Research Station of Chinese Academy of Sciences, Chinese journal of applied ecology, 31, 695-705, 10.13287/j.1001-9332.202003.040, 2020.

Gerken, T., Chamecki, M., and Fuentes, J. D.: Air-Parcel Residence Times Within Forest Canopies, Boundary-Layer Meteorology, 165, 29-54, 10.1007/s10546-017-0269-7, 2017.

Grant, E. R., Ross, A. N., Gardiner, B. A., and Mobbs, S. D.: Field Observations of Canopy Flows over Complex Terrain, Boundary-Layer Meteorology, 156, 231-251, 10.1007/s10546-015-0015-y, 2015.

Gu, L., Massman, W. J., Leuning, R., Pallardy, S. G., Meyers, T., Hanson, P. J., Riggs, J. S., Hosman, K. P., and Yang, B.: The fundamental equation of eddy covariance and its application in flux measurements, Agricultural and Forest Meteorology, 152, 135-148, 10.1016/j.agrformet.2011.09.014, 2012.

Heinesch, B., Yernaux, M., and Aubinet, M.: Some methodological questions concerning advection measurements: a case study, Boundary-Layer Meteorology, 122, 457–478, 10.1007/s10546-006-9102-4, 2007.

Hollinger, D. Y. and Richardson, A. D.: Uncertainty in eddy covariance measurements and its application to physiological models, Tree Physiol, 25, 873-885, DOI 10.1093/treephys/25.7.873, 2005.

Huang, N. E. and Wu, Z.: A review on Hilbert-Huang transform: Method and its applications to geophysical studies, Reviews of Geophysics, 46, 10.1029/2007rg000228, 2008.

Huang, N. E., Shen, Z., Long, S. R., Wu, M. C., Shih, H. H., Zheng, Q., Yen, N.-C., Tung, C. C., and Liu, H. H.: The empirical mode decomposition and the Hilbert spectrum for nonlinear and non-stationary time series analysis, Proceedings of the Royal Society of London. Series A: Mathematical, Physical and Engineering Sciences, 454, 903-995, 10.1098/rspa.1998.0193, 1998.

Khélifa, N., Lecollinet, M., and Himbert, M.: Molar mass of dry air in mass metrology, Measurement, 40, 779-784, 10.1016/j.measurement.2006.05.009, 2007.

Leuning, R., Zegelin, S. J., Jones, K., Keith, H., and Hughes, D.: Measurement of horizontal and vertical advection of CO_2 within a forest canopy, Agricultural and Forest Meteorology, 148, 1777-1797, 10.1016/j.agrformet.2008.06.006, 2008.

Li, S., Yan, Q., Liu, Z., Wang, X., Yu, F., Teng, D., Sun, Y., Lu, D., Zhang, J., Gao, T., and Zhu, J.: Seasonality of albedo and fraction of absorbed photosynthetically active radiation in the temperate secondary forest ecosystem: A comprehensive observation using Qingyuan Ker towers, Agricultural and Forest Meteorology, 333, 10.1016/j.agrformet.2023.109418, 2023.

Li, Y.-C., Liu, F., Wang, C.-K., Gao, T., and Wang, X.-C.: Carbon budget estimation based on different methods of CO_2 storage flux in forest ecosystems, Chinese journal of applied ecology, 31, 3665-3673, 10.13287/j.1001-9332.202011.004, 2020.

Loke, L. H. L. and Chisholm, R. A.: Measuring habitat complexity and spatial heterogeneity in ecology, Ecology Letters, 25, 2269-2288, 10.1111/ele.14084, 2022.

Marcolla, B., Cobbe, I., Minerbi, S., Montagnani, L., and Cescatti, A.: Methods and uncertainties in the experimental assessment of horizontal advection, Agricultural and Forest Meteorology, 198-199, 62-71, 10.1016/j.agrformet.2014.08.002, 2014.

McHugh, I. D., Beringer, J., Cunningham, S. C., Baker, P. J., Cavagnaro, T. R., Mac Nally, R., and Thompson, R. M.: Interactions between nocturnal turbulent flux, storage and advection at an "ideal" eucalypt woodland site, Biogeosciences, 14, 3027-3050, 10.5194/bg-14-3027-2017, 2017.

McMaster, G. S. and Wilhelm, W. W.: Growing degree-days: one equation, two interpretations, Agricultural and Forest Meteorology, 87, 291-300, Doi 10.1016/S0168-1923(97)00027-0, 1997.

Metzger, S.: Surface-atmosphere exchange in a box: Making the control volume a suitable representation for in-situ observations, Agricultural and Forest Meteorology, 255, 68-80, 10.1016/j.agrformet.2017.08.037, 2018.

Montagnani, L., Grunwald, T., Kowalski, A., Mammarella, I., Merbold, L., Metzger, S., Sedlak, P., and Siebicke, L.: Estimating the storage term in eddy covariance measurements: the ICOS methodology, Int Agrophys, 32, 551-567, 10.1515/intag-2017-0037, 2018.

Montagnani, L., Manca, G., Canepa, E., Georgieva, E., Acosta, M., Feigenwinter, C., Janous, D., Kerschbaumer, G., Lindroth, A., Minach, L., Minerbi, S., Mölder, M., Pavelka, M., Seufert, G., Zeri, M., and Ziegler, W.: A new mass conservation approach to the study of CO_2 advection in an alpine forest, Journal of Geophysical Research, 114, 10.1029/2008jd010650, 2009.

Nadeau, D. F., Pardyjak, E. R., Higgins, C. W., Huwald, H., and Parlange, M. B.: Flow during the evening transition over steep Alpine slopes, Quarterly Journal of the Royal Meteorological Society, 139, 607-624, 10.1002/qj.1985, 2013.

Nicolini, G., Aubinet, M., Feigenwinter, C., Heinesch, B., Lindroth, A., Mamadou, O., Moderow, U., Mölder, M., Montagnani, L., Rebmann, C., and Papale, D.: Impact of CO 2 storage flux sampling uncertainty on net ecosystem exchange measured by eddy covariance, Agricultural and Forest Meteorology, 248, 228-239, 10.1016/j.agrformet.2017.09.025, 2018.

Richardson, A. D., Hollinger, D. Y., Burba, G. G., Davis, K. J., Flanagan, L. B., Katul, G. G., William Munger, J., Ricciuto, D. M., Stoy, P. C., Suyker, A. E., Verma, S. B., and Wofsy, S. C.: A multi-site analysis of random error in tower-based measurements of carbon and energy fluxes, Agricultural and Forest Meteorology, 136, 1-18, 10.1016/j.agrformet.2006.01.007, 2006.

Richardson, A. D., Mahecha, M. D., Falge, E., Kattge, J., Moffat, A. M., Papale, D., Reichstein, M., Stauch, V. J., Braswell, B. H., Churkina, G., Kruijt, B., and Hollinger, D. Y.: Statistical properties of random CO_2 flux measurement uncertainty inferred from model residuals, Agricultural and Forest Meteorology, 148, 38-50, 10.1016/j.agrformet.2007.09.001, 2008.

Sha, J., Zou, J., and Sun, J.: Observational study of land-atmosphere turbulent flux exchange over complex underlying surfaces in urban and suburban areas, SCIENCE CHINA-EARTH SCIENCES, 64, 1050-1064, 10.1007/s11430-020-9783-2, 2021.

Siebicke, L., Steinfeld, G., and Foken, T.: CO_2-gradient measurements using a parallel multi-analyzer setup, Atmospheric Measurement Techniques, 4, 409-423, 10.5194/amt-4-409-2011, 2011.

Taud, H. and Parrot, J.-F.: Measurement of DEM roughness using the local fractal dimension, Géomorphologie : relief, processus, environnement, 11, 327-338, 10.4000/geomorphologie.622, 2005.

van Gorsel, E., Harman, I. N., Finnigan, J. J., and Leuning, R.: Decoupling of air flow above and in plant canopies and gravity waves affect micrometeorological estimates of net scalar exchange, Agricultural and Forest Meteorology, 151, 927-933, 10.1016/j.agrformet.2011.02.012, 2011.

Wang, J., Shi, T., Yu, D., Teng, D., Ge, X., Zhang, Z., Yang, X., Wang, H., and Wu, G.: Ensemble machine-learning-based framework for estimating total nitrogen concentration in water using drone-borne hyperspectral imagery of emergent plants: A case study in an arid oasis, NW China, Environmental Pollution, 266, 10.1016/j.envpol.2020.115412, 2020.

Wang, X., Wang, C., Guo, Q., and Wang, J.: Improving the CO_2 storage measurements with a single profile system in a tall-dense-canopy temperate forest, Agricultural and Forest Meteorology, 228-229, 327-338, 10.1016/j.agrformet.2016.07.020, 2016.

Warton, D. I., Duursma, R. A., Falster, D. S., and Taskinen, S.: smatr 3- an R package for estimation and inference about allometric lines, Methods in Ecology and Evolution, 3, 257-259, 10.1111/j.2041-210X.2011.00153.x, 2012.

Webb, E. K., Pearman, G. I., and Leuning, R.: Correction of flux measurements for density effects due to heat and water vapour transfer, Quarterly Journal of the Royal Meteorological Society, 106, 85-100, 10.1002/qj.49710644707, 1980.

Xu, K., Pingintha-Durden, N., Luo, H., Durden, D., Sturtevant, C., Desai, A. R., Florian, C., and Metzger, S.: The eddy-covariance storage term in air: Consistent community resources improve flux measurement reliability, Agricultural and Forest Meteorology, 279, 10.1016/j.agrformet.2019.107734, 2019.

Yang, B., Hanson, P. J., Riggs, J. S., Pallardy, S. G., Heuer, M., Hosman, K. P., Meyers, T. P., Wullschleger, S. D., and Gu, L.-H.: Biases of CO2 storage in eddy flux measurements in a forest pertinent to vertical configurations of a profile system and CO2 density averaging, Journal of Geophysical Research, 112, 10.1029/2006jd008243, 2007.

Yang, P. C., Black, T. A., Neumann, H. H., Novak, M. D., and Blanken, P. D.: Spatial and temporal variability of CO_2 concentration and flux in a boreal aspen forest, J Geophys Res-Atmos, 104, 27653-27661, Doi 10.1029/1999jd900295, 1999.

Yao, Y., Zhang, Y., Yu, G., Song, Q., Tan, Z., and Zhao, J.: Estimation of CO_2 storage flux between forest and atmosphere in a tropical forest, Journal of Beijing Forestry University, 33, 23-29, 2011.

Zhang, M., Wen, X., Yu, G.-r., Zhang, L.-m., Fu, Y., Sun, X., and Han, S.-j.: Effects of CO_2 storage flux on carbon budget of forest ecosystem, Chinese journal of applied ecology, 21, 1201-1209, 2010.

Zhu, J., Gao, T., Yu, L., Yu, F., Yang, K., Lu, D., Yan, Q., Sun, Y., Liu, L., Xu, S., Zhang, J., Zheng, X., Song, L., and Zhou, X.: Functions and Applications of Multi-tower Platform of Qingyuan Forest Ecosystem Research Station of Chinese Academy of Sciences (Qingyuan Ker Towers), Bulletin of the Chinese Academy of Sciences, 36, 351-361, 10.16418/j.issn.1000-3045.20210304002, 2021.